Technical Report

R 758

NAVAL CIVIL ENGINEERING LABORATORY
Port Hueneme, California 93043

Sponsored by
DEFENSE NUCLEAR AGENCY

February 1972 DASA SC 318

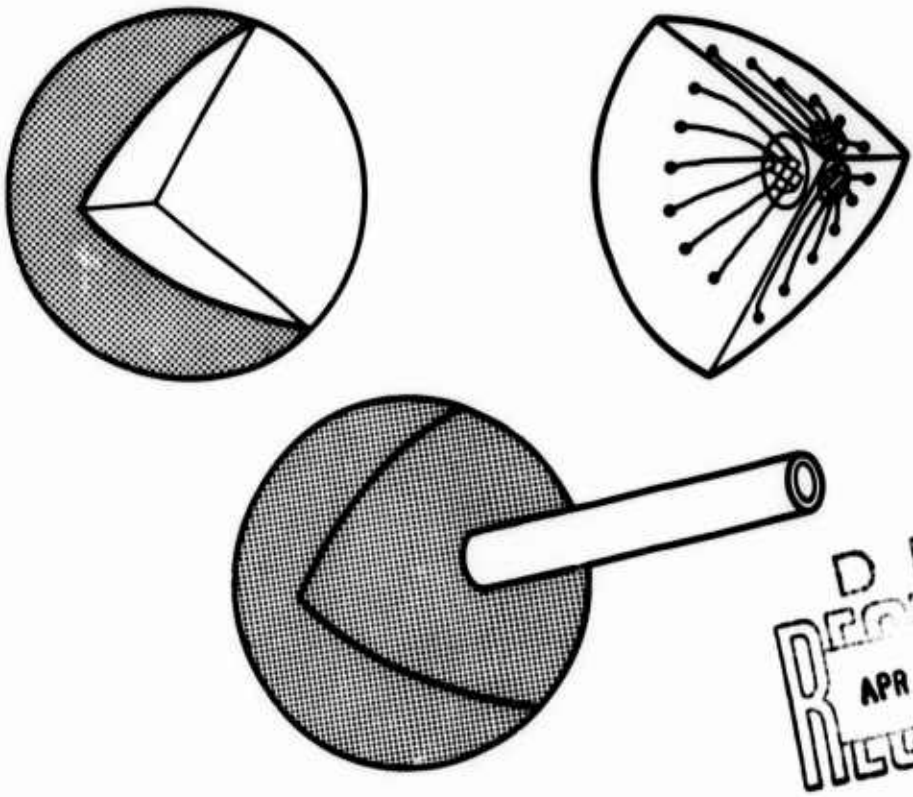

EVALUATION OF A THREE-DIMENSIONAL STRESS CELL FOR GRANULAR SOILS

EVALUATION OF A THREE-DIMENSIONAL STRESS CELL FOR GRANULAR SOILS

Technical Report R-758

YF-008-08-02-108, SC318

by

T. K. Lew

ABSTRACT

This study presents the results of tests of rigid, solid, spherical, three-dimensional stress cells for measuring the complete state of stress at a point in a soil field under static or dynamic loading. In addition, a theory is presented for defining the behavior of a spherical stress cell embedded in nonlinear materials. The test results indicate that the stress cells are excellent for making static measurements in sand but that their adequacy for dynamic measurements requires further evaluation.

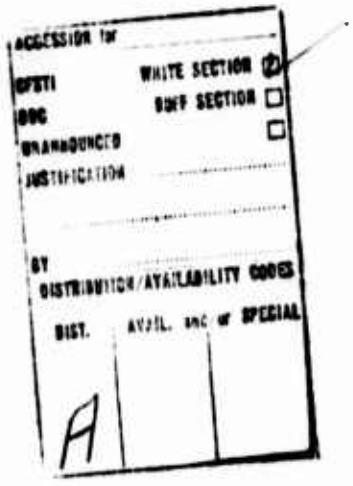

Unclassified
Security Classification

DOCUMENT CONTROL DATA - R & D

(Security classification of title, body of abstract and indexing annotation must be entered when the overall report is classified)

1. ORIGINATING ACTIVITY (Corporate author) Naval Civil Engineering Laboratory Port Hueneme, California 93043	2a. REPORT SECURITY CLASSIFICATION Unclassified 2b. GROUP

3. REPORT TITLE

EVALUATION OF A THREE-DIMENSIONAL STRESS CELL FOR GRANULAR SOILS

4. DESCRIPTIVE NOTES (Type of report and inclusive dates)

Not final; July 1970 to June 1971

5. AUTHOR(S) (First name, middle initial, last name)

T. K. Lew

6. REPORT DATE	7a. TOTAL NO. OF PAGES	7b. NO. OF REFS
February 1972	65	10

8a. CONTRACT OR GRANT NO. SC318 b. PROJECT NO. YF-008-08-02-108 c. d.	9a. ORIGINATOR'S REPORT NUMBER(S) TR-758 9b. OTHER REPORT NO(S) (Any other numbers that may be assigned this report)

10. DISTRIBUTION STATEMENT

Approved for public release; distribution unlimited.

11. SUPPLEMENTARY NOTES	12. SPONSORING MILITARY ACTIVITY Defense Nuclear Agency Washington, D. C. 20305

13. ABSTRACT

This study presents the results of tests of rigid, solid, spherical, three-dimensional stress cells for measuring the complete state of stress at a point in a soil field under static or dynamic loading. In addition, a theory is presented for defining the behavior of a spherical stress cell embedded in nonlinear materials. The test results indicate that the stress cells are excellent for making static measurements in sand but that their adequacy for dynamic measurements requires further evaluation.

DD FORM 1 NOV 68 1473 (PAGE 1)

S/N 0101-807-6801

Unclassified
Security Classification

14 KEY WORDS	LINK A		LINK B		LINK C	
	ROLE	WT	ROLE	WT	ROLE	WT
Solid, spherical stress cell						
Soils						
Static stress measurements						
Dynamic stress measurements						
Stress cells						

CONTENTS

INTRODUCTION

Purpose and Scope

The purpose of this research is to evaluate the response of rigid, solid, spherical stress cells developed at the Naval Civil Engineering Laboratory (NCEL) to measure the complete state of stress at a point in a granular soil. A theory defining the behavior of spherical stress cells embedded in materials having nonlinear properties is presented. Results of tests on four stress cells made from phenolic plastic billiard balls (cue balls) are reported. Each of the four stress cells was tested hydrostatically in water and statically in a well-graded sand. Two of the stress cells were tested in beach sand under a high-explosive environment at the Naval Missile Center, Point Mugu, California. In addition, results from dynamic tests of one stress cell that was tested during the preliminary evaluation[1] are presented. This study was sponsored by the Defense Nuclear Agency (formerly the Defense Atomic Support Agency).

Analysis of Problem

One of the deterrents to further advances in understanding the interaction between a buried structure and the soil is the lack of knowledge about the induced stresses—particularly those near the buried structure. Gaining such information requires a reliable soil stress cell. Unfortunately, accurate measurement of soil stresses is difficult because soil stress gages generally do not behave like the soil they replace. Furthermore, the soil surrounding the gage is disturbed during installation, and the behavior of the recompacted soil is different from that of the undisturbed soil.

Most stress gages measure normal stresses in one direction only and do not respond accurately on unloading. In addition, no existing gage can accurately measure the shear stress in a soil field. Most soil gages consist of a flexible diaphragm supported on a rigid base. Measured deformation or strain of the diaphragm from such a gage is related theoretically to the applied pressure. Because of mechanical imperfections induced during fabrication, the gages are usually calibrated under uniform, externally applied fluid pressure to account for the difference between theoretical and actual gage behavior.

The accuracy of stress measurements from a soil gage depends on the interaction between the gage and the soil. When embedded in soil, the gage will act as a stiff inclusion, a soft inclusion, or a combination of the two, depending upon the relative stiffness between the gage and the soil. A soft inclusion causes the stresses in the soil field to move away from the inclusion, whereas a stiff inclusion attracts stresses in the soil field. As is well known, the modulus of deformation of soil is not a unique value, even for a single soil; it varies with stress level, relationship between lateral and normal stresses, moisture content, rate of loading, and other parameters. The effective modulus of deformation for a soil gage, by contrast, usually is a constant within its range of operation. The modular ratio (the ratio of the modulus of soil stress gage to the modulus of the soil in which the gage is embedded) changes with the magnitude of loading—a change which has a marked effect on the gage response. Consequently, the registration ratio of a gage (the ratio of the gage output while embedded in soil under a known pressure to the output of the same gage when subjected to an identical fluid pressure) decreases as the soil stiffness increases. Gages are commonly embedded in soil and calibrated in the laboratory to account for changes in registration ratio. Even under controlled laboratory conditions, however, gage response is highly sensitive to gage embedment procedures.

In short, the response of soil stress gages is usually sensitive to methods of installation, to changes in soil stiffness, and to other soil properties that vary with load. There is a need for a gage that is insensitive to these factors. The following paragraphs present a theoretical bases and the evaluation of a three-dimensional (3-D) soil gage that meets most of the indicated requirements.

Background

In 1949, Coutinho presented a theory relating the principal stresses in a relatively rigid spherical inclusion to those in the encompassing solid (host material).[2] Coutinho's solution was based on Goodier's closed-formed elastic solution for a sphere embedded in an infinite solid.[3] According to Coutinho, the stress concentration factor for the inclusion is essentially a constant if the modulus of elasticity is four or five times the corresponding value for the surrounding solid. He suggested that the theory be used to develop a stress cell for use in freshly poured concrete. Such a cell would be useful because the stiffness properties of the concrete during the hardening of the cement are not known.

If the principal stresses and their directions in the host material are known, Coutinho's theory can be applied to obtain stress measurements in materials having nonlinear stiffness properties. Unfortunately, the principal stresses and their directions are generally not known beforehand in most experiments. The application of Coutinho's theory, therefore, is limited to situations where the principal stresses and their directions are known.

In 1969, the author developed a theory that relates the complete state of stress inside a spherical inclusion to the corresponding state of stress in the host elastic solid through use of results from the finite element analyses of a spherical inclusion embedded in an elastic solid. Subsequently, a stress cell was fabricated from plastic cue balls and subjected to static and dynamic tests. Results from the preliminary tests[1] were encouraging, but because the test results were for one stress cell only, the preliminary test results were not considered conclusive.

Approach

The solid sphere was chosen because its response is independent of its placement orientation. It has no sharp corners to cause stress gradients within itself. Furthermore, strains near the center of the solid sphere are not sensitive to localized loads on the outer surface of the sphere.

A spherical stress cell will act as a rigid or a soft inclusion, depending on the relative stiffness between the stress cell and the surrounding soil. If the stress cell is made from a relatively low-modulus material, measured deformations of the cell along selected directions must be related to corresponding stresses in the soil. Such a relationship can be established only by elaborate laboratory calibrations. The stress relief factor (the ratio of the stress in the inclusion to the corresponding stress in the soil) for a low-modulus inclusion is very sensitive to changes in soil modulus, which varies with the state of stress in the soil. This sensitivity makes laboratory calibration very difficult, if not impractical. Furthermore, a low-modulus material will not offer sufficient protection against shock to the fragile sensing elements when the stress cell is used to obtain dynamic measurements. The foregoing considerations preclude the use of low-modulus material for a stress gage. Rather, a relatively rigid material appears to offer more promise.

THEORY

Finite Element Analysis

Analyses of a sphere embedded in a solid were performed by using a linear elastic, finite element computer program for axisymmetric structures.[4] The solid and the inclusion were assumed to be linear elastic, isotropic, and homogeneous throughout the analyses. Furthermore, the solid was idealized as a cylinder with a sphere embedded in its center (Figure 1). Outer boundaries of the cylinder were located far enough away from the surface of the inclusion that the inclusion would respond as if it were embedded in an infinite solid. Because of structural symmetry, only one quadrant of the cross-sectional area was analyzed. The solid and the inclusion were idealized as an assemblage of quadrilateral ring elements. Ninety ring elements (not shown on Figure 1) were used to represent the spherical inclusion to ensure good definition of stress variation. Continuous displacements were maintained along all element boundaries. The inclusion was assigned a modulus of elasticity E_c and a Poisson's ratio ν_c.* Corresponding values assigned to the solid were E_h and ν_h. The idealized structure was loaded with a uniformly distributed pressure on top in the **Z**-direction. Displacements at the nodal points and the stresses at the center of each element were printed by the computer from the output of the finite element program.

A series of solutions for the solid–inclusion problem were obtained by holding the modulus of elasticity and Poisson's ratio for the inclusion constant and varying the corresponding values for the solid. Results of these calculations indicate that the inclusion has negligible influence on the stresses in the cylinder at radial distances (measured from the surface of the inclusion) greater than five times the inclusion radius. The shear stress within the inclusion is zero. Furthermore, the stress along any direction in the inclusion is a constant and does not vary with radial distance.

From the results, a family of stress concentration curves were obtained for the solid–inclusion problem (Figures 2 and 3). The direct stress concentration factors, C_s (shown in Figure 2) were obtained by dividing the normal stress in the inclusion in the direction of the applied load by the applied stress. The lateral stress concentration factors, C_c (shown in Figure 3) were obtained by dividing the stress in the inclusion in a direction normal to the applied load by the applied stress.

---

*See foldout list of symbols after References.

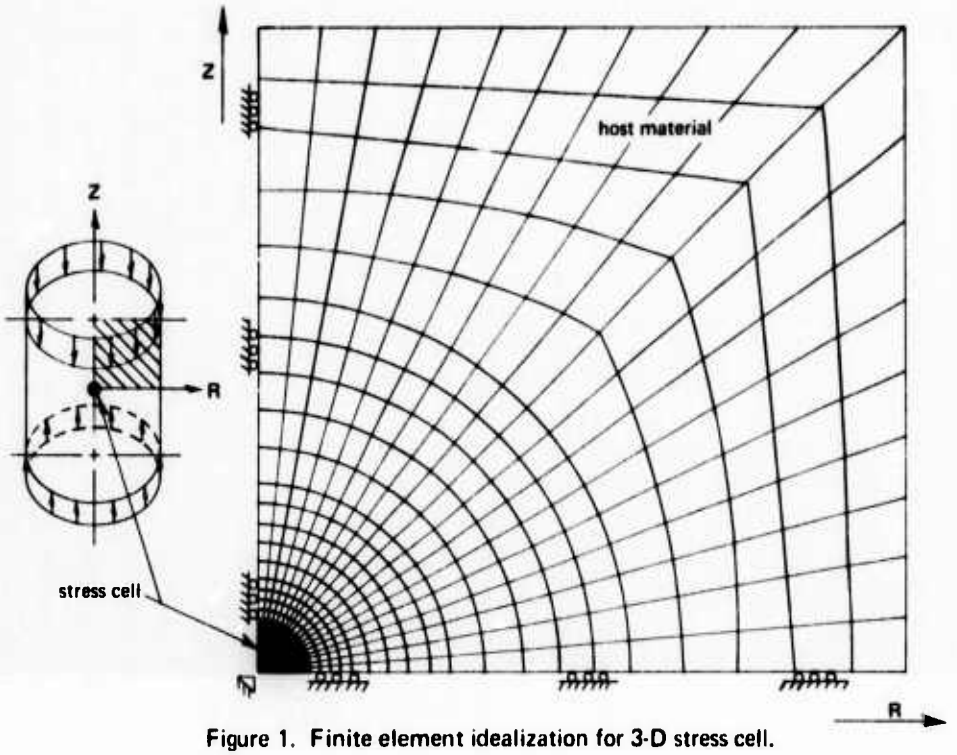

Figure 1. Finite element idealization for 3-D stress cell.

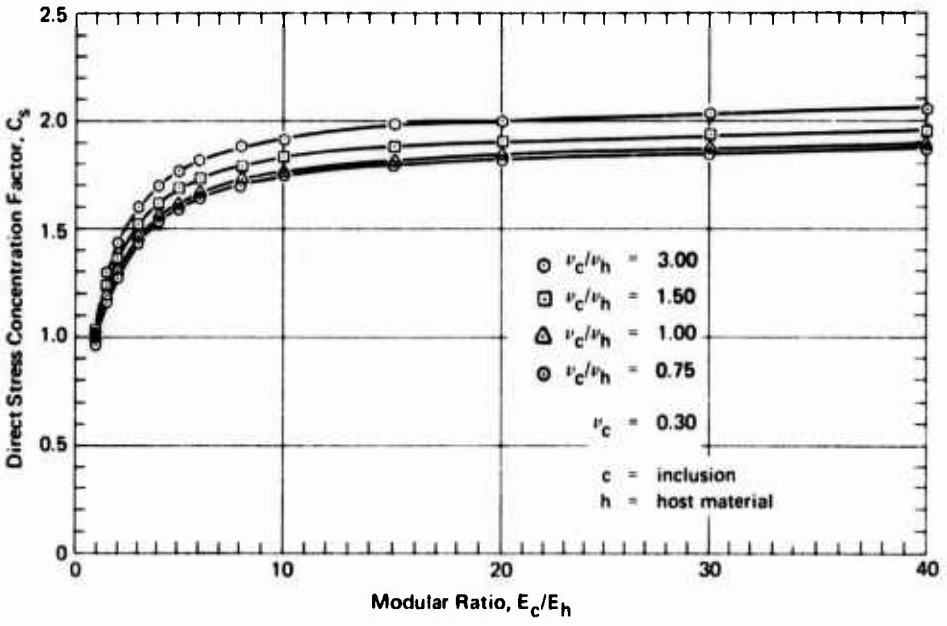

Figure 2. Direct stress concentration factor, C_s.

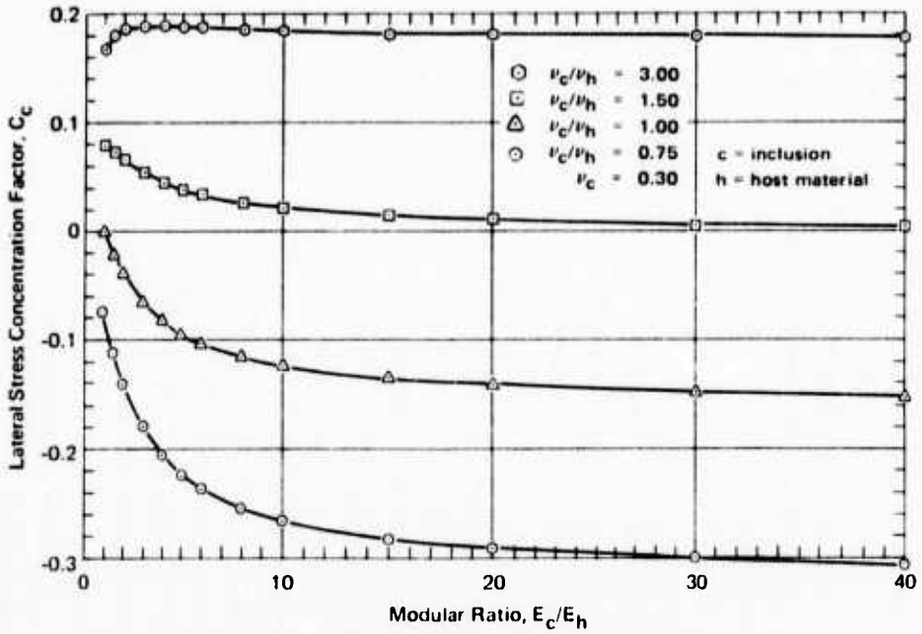

Figure 3. Lateral stress concentration factor, C_c.

The stress concentration curves in Figures 2 and 3 show that the stress concentration factors are insensitive to changes in stiffness of the solid for modular ratios E_c/E_h greater than 10. This means that stress measurements obtained from a spherical stress cell (made from a material having a modulus of elasticity about 10 times larger than the maximum soil modulus) in soil will not be affected by changes in the soil modulus. However, the following assumption must first be made: The instantaneous stiffness properties of a given soil can be represented by a modulus of elasticity and a Poisson's ratio. This assumption should be valid for most soils and materials that exhibit nonlinear stiffness properties, because any nonlinear stress–strain curve may be approximated by a series of short linear segments.

The stress concentration curves can be used as the basis for developing a 3-D stress cell. Understandably, the spherical stress cell must be made from a material that (1) responds linearly and elastically in the loading range considered and (2) has a modulus of elasticity about 10 times larger than the maximum effective soil modulus in the same loading range. A stress cell with these features would require no calibration. A theory that relates the complete state of stress in the inclusion to that in the soil must be established.

Development of Theory

Stress–Strain Relationship for Spherical Inclusion. The complete state of stress in the inclusion can be determined from six independent strain components. In a rectangular coordinate system, the stress and strain components at a point in a continuum are related by:

$$\sigma_{Xc} = \lambda e + 2G\epsilon_X \quad (1)$$

$$\sigma_{Yc} = \lambda e + 2G\epsilon_Y \quad (2)$$

$$\sigma_{Zc} = \lambda e + 2G\epsilon_Z \quad (3)$$

$$\tau_{XYc} = G\gamma_{XY} \quad (4)$$

$$\tau_{YZc} = G\gamma_{YZ} \quad (5)$$

$$\tau_{ZXc} = G\gamma_{ZX} \quad (6)$$

where $\sigma_{Xc}, \sigma_{Yc}, \sigma_{Zc}$ = normal stress components

$\tau_{XYc}, \tau_{YZc}, \tau_{ZXc}$ = shear stress components

$\epsilon_X, \epsilon_Y, \epsilon_Z$ = normal strain components

$\gamma_{XY}, \gamma_{YZ}, \gamma_{ZX}$ = shear strain components

e = volumetric strain, $e = \epsilon_X + \epsilon_Y + \epsilon_Z$

G = shear modulus, $G = \dfrac{E_c}{2(1 + \nu_c)}$

λ = Lamé's constant $= \dfrac{\nu_c E_c}{(1 + \nu_c)(1 - 2\nu_c)}$

ν_c = Poisson's ratio for inclusion

E_c = Young's modulus for inclusion

Relationship Between Normal Stresses in Inclusion and Those in Host Material. Consider the special case of an elastic solid with a sphere embedded in its center, and the solid subjected to the combined action of uniform, normal stresses σ_{Xh}, σ_{Yh}, and σ_{Zh} of arbitrary magnitudes in the direction of each of the reference axes. The state of stress in the inclusion can be obtained from the finite element solutions by applying the principle of superposition. Accordingly, normal stresses induced in the inclusion from the application of normal stresses σ_{Xh}, σ_{Yh}, and σ_{Zh}, were summed to give:

$$\sigma_{Xc} = C_s\sigma_{Xh} + C_c(\sigma_{Yh} + \sigma_{Zh}) \quad (7)$$

$$\sigma_{Yc} = C_s\sigma_{Yh} + C_c(\sigma_{Xh} + \sigma_{Zh}) \quad (8)$$

$$\sigma_{Zc} = C_s\sigma_{Zh} + C_c(\sigma_{Xh} + \sigma_{Yh}) \quad (9)$$

The variables C_s and C_c are the direct and lateral stress concentration factors, respectively. No shear stresses are induced in the inclusion from the application of normal stresses. By solving Equations 7, 8, and 9 for the normal stresses in the host material, the following equations are obtained:

$$\sigma_{Xh} = K\sigma_{Xc} + k(\sigma_{Yc} + \sigma_{Zc}) \quad (10)$$

$$\sigma_{Yh} = K\sigma_{Yc} + k(\sigma_{Xc} + \sigma_{Zc}) \quad (11)$$

$$\sigma_{Zh} = K\sigma_{Zc} + k(\sigma_{Xc} + \sigma_{Yc}) \quad (12)$$

$$K = \frac{C_s + C_c}{C_s^2 + C_sC_c - 2C_c^2} \quad (13)$$

$$k = \frac{-C_c}{C_s^2 + C_sC_c - 2C_c^2} \quad (14)$$

The constants **K** and **k** are designated as the direct–normal, and lateral–normal stress influence coefficients, respectively. Equations 10, 11, and 12 define the relationship between the normal stresses in the host material and the corresponding values in the inclusion. In completing the relationship of the complete state of stress in the host material and in the inclusion, the relationship between the shear stresses in the host material and those in the inclusion must be established.

Relationship between shear stress in inclusion and those in host material. The relationship between the shear stresses in the inclusion and those in the hose material can be established from Equations 10, 11, and 12 and the law of stress transformation. According to this law, a plane state of pure shear is the equivalent of a plane state of normal stress (see Figure 4) provided that :

$$\tau_{XY} = \sigma_{X'} = -\sigma_{Y'}$$

For the inclusion, designated by subscript **c**, and the hose material, designated by the subscript **h**, this relationship can be expressed as:

$$\tau_{XYc} = \sigma_{X'c} = -\sigma_{Y'c} \tag{15}$$

$$\tau_{XYh} = \sigma_{X'h} = -\sigma_{Y'h} \tag{16}$$

By substituting Equations 15 and 16 into Equations 10, 11, and 12 for the special case of a plane state of pure shear in the host material,

where

$$\tau_{XYh} \neq 0$$

$$\tau_{YZh} = \tau_{ZXh} = \sigma_{Xh} = \sigma_{Yh} = \sigma_{Zh} = 0$$

the following relationship between the shear stress in the inclusion and that in the host material is obtained:

$$\tau_{XYh} = K_s \tau_{XYc} \tag{17}$$

where

$$K_s = K - k \tag{18}$$

Here, K_s is designated as the shear stress influence coefficient. Similarly, it can be shown that

$$\tau_{YZh} = K_s \tau_{YZc} \tag{19}$$

$$\tau_{ZXh} = K_s \tau_{ZXc} \tag{20}$$

The values of **K**, **k**, and K_s are presented in Figures 5, 6, and 7 to facilitate future computations.

In summary, the complete state of stress at a given point in the host material can be computed from strain measurements of the inclusion using Equations 1 through 6 and 10 through 20 without having detailed knowledge of the stiffness properties of the nonlinear host material.

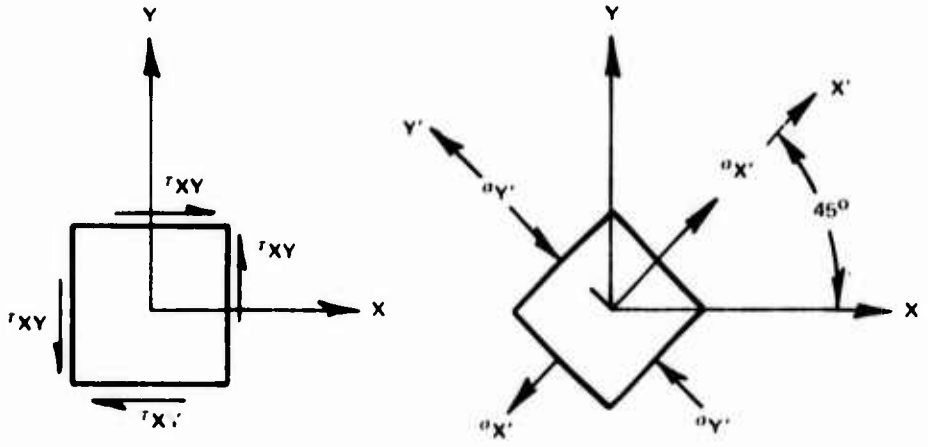

Figure 4. Plane state of pure shear.

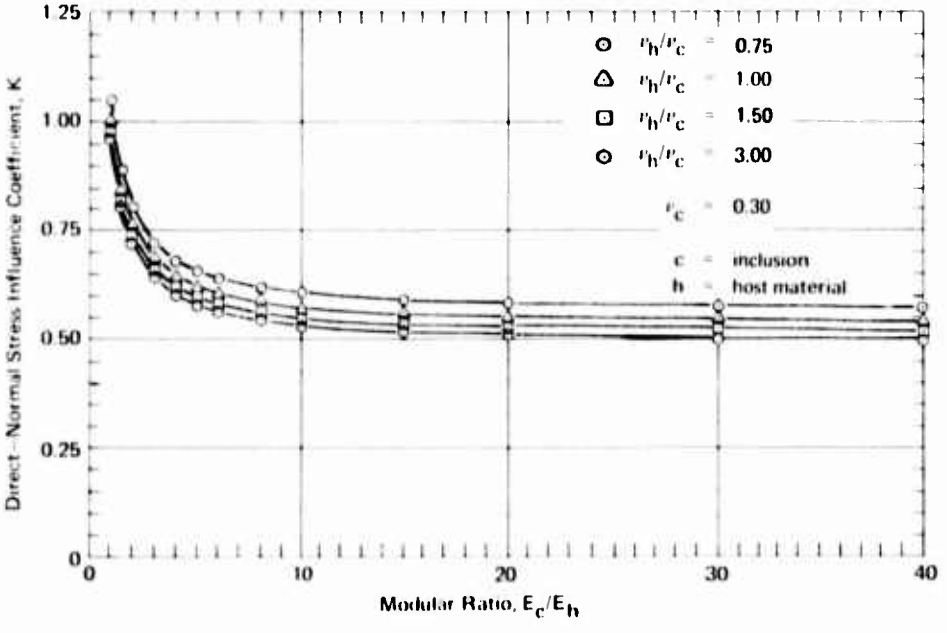

Figure 5. Direct-normal stress influence coefficient, K.

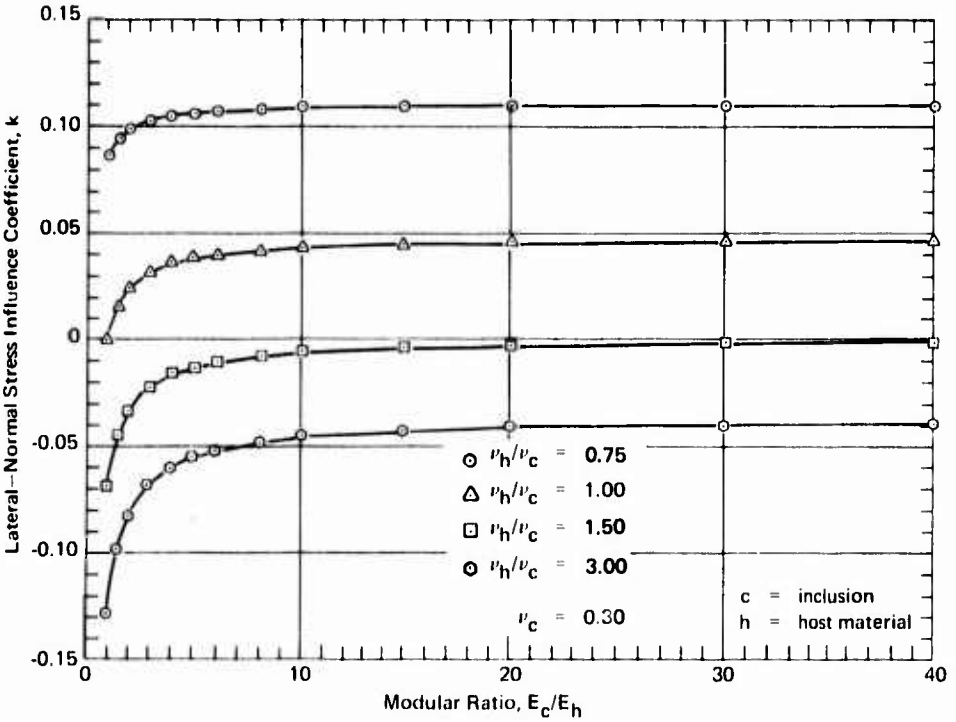

Figure 6. Lateral–normal stress influence coefficient, k.

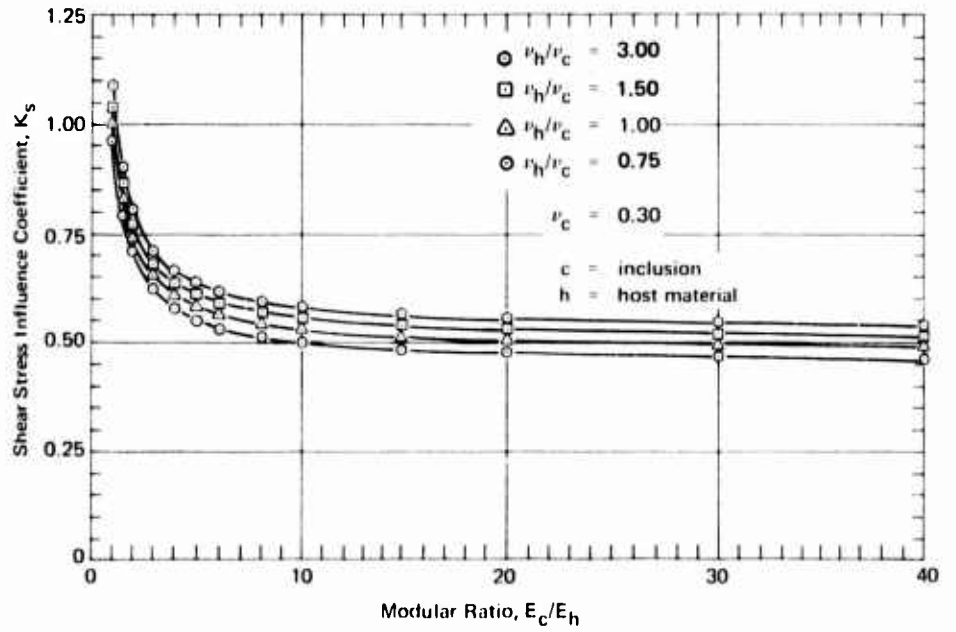

Figure 7. Shear stress influence coefficient, K_s.

DESIGN AND FABRICATION

Design Considerations

The most important factor in the design of a stress cell is its stiffness. During the derivation of the theory, it was assumed that the stress cell is fabricated from a linear elastic material having a modulus of elasticity about 10 times larger than the maximum modulus of deformation of the soil. For most granular soils (sand) the upper limit for the static modulus (one-dimensional confined) of interest for virgin loading is about 40×10^3 psi. Thus, the stress cell must have a modulus of about 400×10^3 psi.

There is no advantage, however, in using a material with a modulus of elasticity much larger than 400×10^3 psi, because for modular ratios greater than 10, the sensitivity of the stress cell decreases as its modulus increases. The Poisson's ratio for the stress cell material need not be considered, because, as shown in Figures 2 and 3, the Poisson's ratio has little influence on the response of the stress cell.

The relative density of the stress cell with respect to the soil and its frequency response can have a large influence on the accuracy of dynamic measurements. Input wave shapes, for instance, will be distorted if the natural frequency of the stress cell is low compared with the effective frequency response of the soil. Thus, the stress cell should have a much higher frequency response than the surrounding soil. This requirement is automatically satisfied by meeting the modulus of elasticity requirement.

If the densities of the stress cell and the soil are different, apparent dynamic stresses will be induced in the cell from the difference in inertial forces between the two bodies. Such an undesirable effect can be minimized by matching the density of the stress cell and the soil as closely as possible.

Size irregularities in the soil particles near the stress cell can cause the cell to give erroneous measurements if the size of the stress cell is small compared to the maximum dimensions of the soil particle irregularities. The diameter of the stress cell, consequently, should be large compared to the maximum dimensions of soil irregularities. The stress cell will then measure only the average state of stress at a point in soil.

Six independent stress components, three normal and three shear, are required to define the complete state of stress at interior points of elastic, homogeneous, and isotropic solids. These components must be obtained indirectly from six independent strain measurements, because stress components, in general, cannot be measured directly. The required strain measurements can be made by using foil resistance or semiconductor strain gages, depending on the sensitivity desired. Strain gages, however, are fragile and must be protected in a hostile soil environment. They are best

protected by embedment in the stress cell. Studies by Dove, Braiser, and Baker[5] indicate that commercially available strain gages, when embedded in materials with a modulus of elasticity greater than 650 x 10^3 psi, cause negligible disturbances in a static or dynamic strain field. Strain gages, then, can be embedded in the stress cell without causing significant measurement errors if the modulus requirement is satisfied.

The strain gages should be oriented to form a 3-D strain rosette as shown in Figure 8 to minimize the amount of data reduction required. The rosette shown in Figure 8 was adapted from the one used by Dove and Baker[6] by adding one gage (dotted line) on each of the three reference planes. However, the 135-degree gages are redundant and are not normally used unless one or more of the other gages (**X, Y, Z, XY45, ZX45, YZ45**) malfunctions. Shearing strains can be computed from the strain data by applying the following equations:

$$\gamma_{XY} = 2\epsilon_{XY45} - \epsilon_X - \epsilon_Y \quad (21)$$

$$\gamma_{YZ} = 2\epsilon_{YZ45} - \epsilon_Y - \epsilon_Z \quad (22)$$

$$\gamma_{ZX} = 2\epsilon_{ZX45} - \epsilon_Z - \epsilon_X \quad (23)$$

where $\gamma_{XY}, \gamma_{YZ}, \gamma_{ZX}$ = shearing strains in reference planes

$\epsilon_{XY45}, \epsilon_{YZ45}, \epsilon_{ZX45}$ = Measured strains from 45-degree gage in reference planes

$\epsilon_X, \epsilon_Y, \epsilon_Z$ = measured normal strains along reference axes

Alternative setups using the 135-degree gages when one or more of the other gages do not function are presented in the Appendix.

To reduce the number of channels required for dynamic measurements, an FM (frequency modulated) multiplexing unit was specially made for the stress cell. This unit takes six channels of data information and transmits them via one channel.

Fabrication

For this study, four stress cells (SFB-2, SFB-3, SFB-4, and SFB-5) were fabricated from 2-1/4-inch-diameter, phenolic plastic billiard balls (cue balls). These balls have the desired shape and approximately the desired properties: an elastic modulus of 494 x 10^3 psi, a Poisson's ratio

of 0.413, and a density of 109 pcf. First, the female section was formed by cutting approximately one octant from one cue ball (see Figure 9). Then the matching male section was cut from another ball. The dimension along each of the three orthogonal edges was machined to 1.40 inches, 0.275 inch larger than the radius of the ball, so that the approximate center of the rosette would coincide with the center of the ball. A 45-degree strain rosette (1/4-inch gage length, type FABR-25-S13*) was bonded to each of the three orthogonal faces on the male section with Bakelite** cement. These three rosettes formed the 3-D strain rosette shown in Figure 8. Lead wires from the strain gages were threaded through 0.015 inch diameter holes drilled in the male section (Figure 9, section A-A). The small lead wires were soldered to larger lead wires before the male and female sections were bonded together. The solder joints were located about 1/8 inch below the orthogonal faces of the male section. All the large lead wires converged at the handle. These large lead wires were threaded into the handle and encapsulated with epoxy resin when the handle was bonded to the male section. Incidentally, the handle was made from a laminated phenolic plastic. The handle serves as a reference for orienting the stress cell and as a protector for the lead wires.

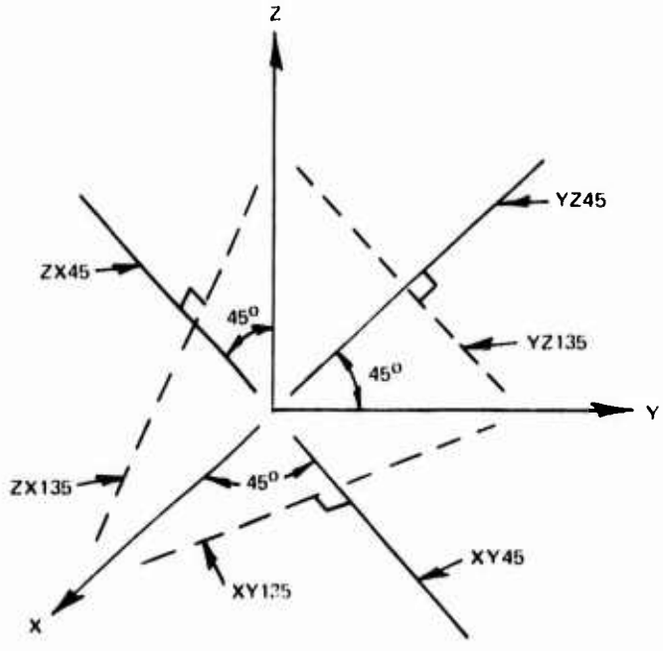

Note: Nine strain gages total, one along each reference axis and two on each reference plane as shown.

Figure 8. Three-dimensional strain rosette.

*Baldwin Lima Hamilton Corporation.

**Union Carbide Corporation.

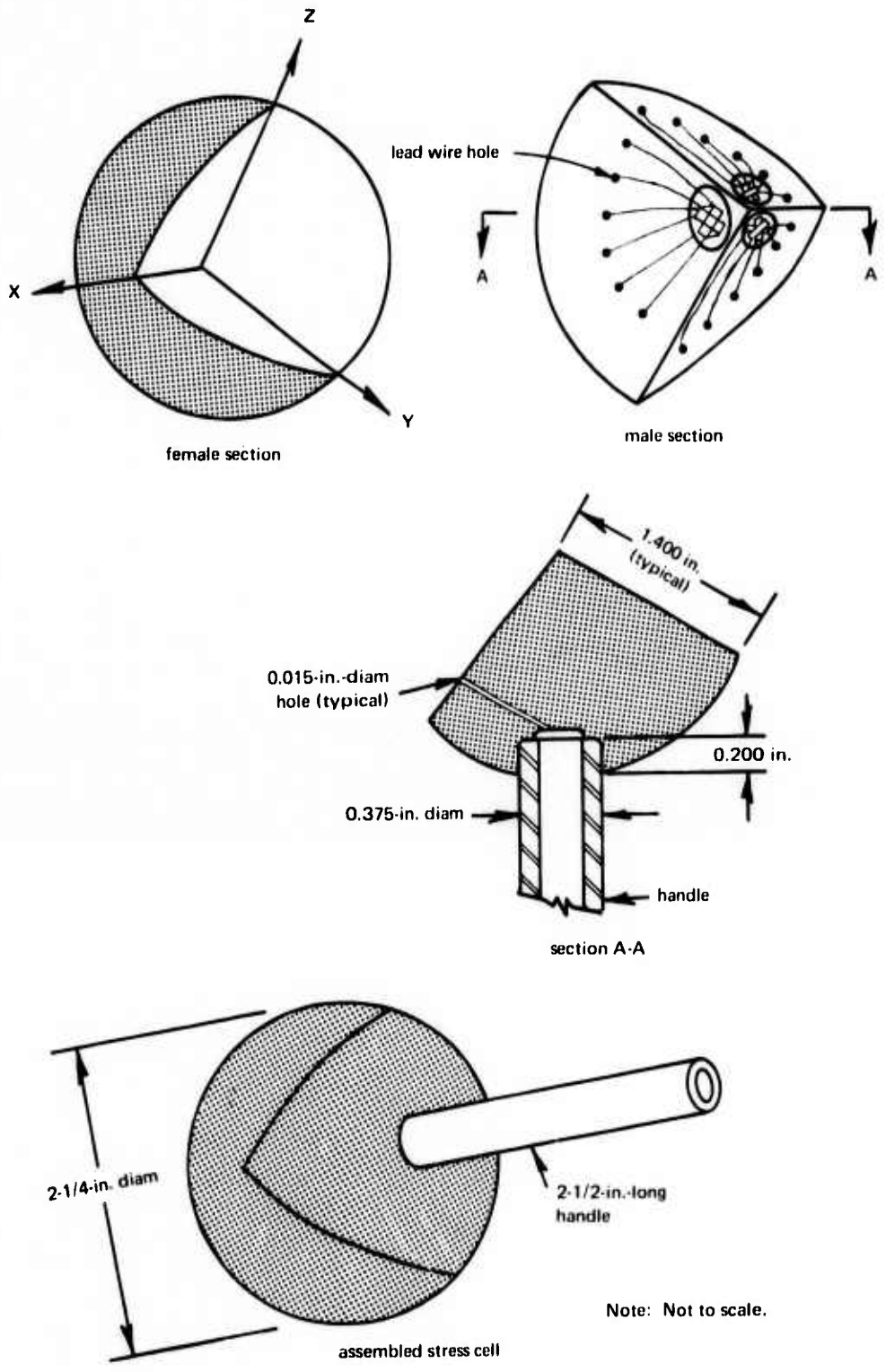

Figure 9. Fabrication of 3-D stress cell.

Next, the male and female sections were bonded together with an epoxy adhesive (EPY* 150), and cured at 150°F for approximately 4 hours. The surface of the assembled stress cell was sanded with fine emery cloth and marked with colored lines identifying the orientation of the strain gages. The assembled cell was then coated with an epoxy adhesive and covered with a layer of 20-30 Ottawa sand to enhance shear transfer. Finally, all the lead wires from the stress cell were shielded with aluminum foil (to eliminate spurious electrical signals induced by electromagnetic pulses) and were covered with shrinkable tubing. Figure 10 shows the assembled stress cell.

EXPERIMENTAL WORK

Introduction

Each of the four stress cells (SFB-2, SFB-3, SFB-4, and SFB-5) was subjected to one hydrostatic test in water and two static normal tests in sand. Stress cells SFB-3, SFB-4, and SFB-5 were subjected to one shear test each. Stress cell SFB-1 was tested dynamically during the preliminary evaluation.[1] Stress cells SFB-3 and SFB-4 were tested dynamically in beach sand at Point Mugu.

The purpose of the hydrostatic test was to check the response of the embedded strain gages. Static response of the stress cell to normal stresses and shear stresses in sand was evaluated in the static normal tests and shear tests, respectively. Only the dynamic response of the stress cell to normal stresses in sand was evaluated in the dynamic tests.

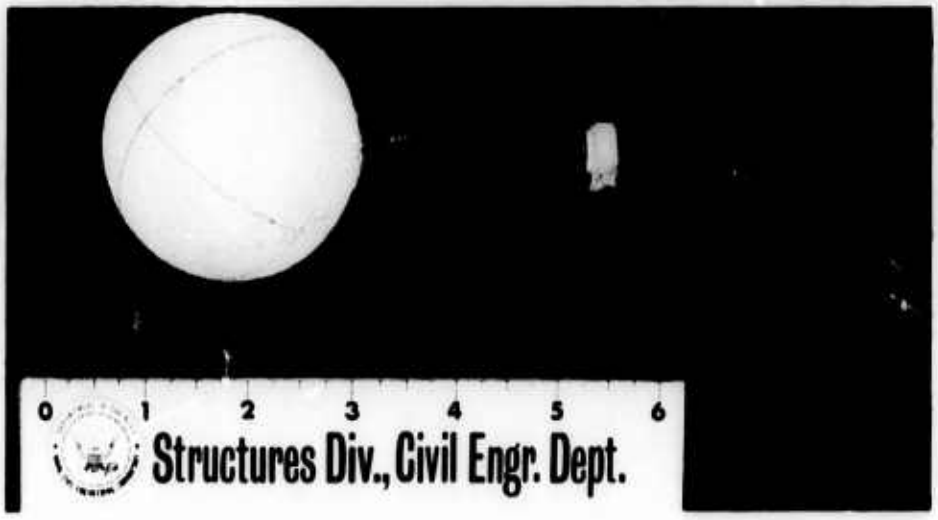

Figure 10. Assembled stress cell.

*Baldwin-Lima-Hamilton Corporation.

Test Procedure

Hydrostatic Tests. Two stress cells at a time were placed in a 20,000-psi-capacity pressure vessel filled with water and subjected to three successive loading cycles to a maximum pressure of 3,000 psi at 100-psi increments. Hydrostatic pressure, measured by a Bourdon pressure gage, was applied externally by a motor-driven air pump. All strain gages within each stress cell were monitored in these tests.

Static Tests. A soil tank (Figure 11) filled with a dry (0.3% moisture), well-graded sand (Figure 12) was used in the static tests. This 36-inch-long tank was made from a 17-1/4-inch-ID (inside diameter), 3/8-inch-wall steel pipe. The sand was obtained from the dry riverbed of the Santa Clara River at Ventura, California. A greased, thin polyethylene liner was used in each test to reduce wall friction. A new liner was used for each test. In-place sand density was controlled by dropping the sand through a funnel into the soil tank from a height of 20 inches in 6-inch lifts. When the sand level reached the midheight of the tank, the stress cell was pressed about 3/4 inch into the sand. In the normal tests, the stress cell was oriented such that its **Z**-strain gage coincided with the axis of the tank. In the shear tests, the stress cell was so oriented that the **YZ45**-strain gage of the stress cell coincided with the axis of the tank. Subsequently, more sand was sifted around the stress cell through the funnel. Special care was taken to prevent the sand from bouncing off the stress cell to minimize the possibility of segregation of sand particles. This procedure was repeated for two 1-inch lifts until the cell was completely covered. Filling of the tank was resumed, as in the bottom half. Sand densities in the tests varied between 102.5 to 107.8 pcf. The average density was 105.5 pcf.

In each test, the sand in the tank was loaded with a 400-kip testing machine in 85.6 psi increments to a maximum pressure of 1,110 psi through three cycles. Time between load increments during loading was about 30 seconds. The maximum load was held for 3 minutes. During unloading, the load was removed in 171.2-psi increments at about 1 minute per load increment. Vertical displacement of the sand at the top of the tank was measured with a linear potentiometer attached to the steel loading plate on the top of the soil tank. Four pairs of strain gages were placed, equally spaced, around the circumference at the midheight on the outside of the soil tank (Figure 11) to measure strains for computing the lateral stresses in the sand at the level of the stress cell. Each pair consisted of a vertical gage and a hoop gage for measuring the vertical strain and hoop strain in the soil tank.

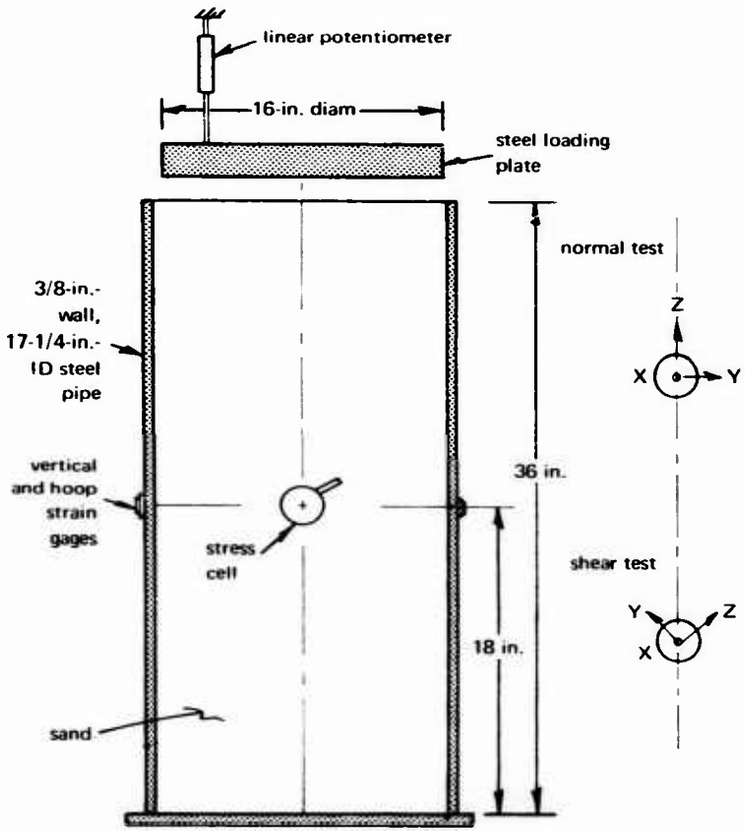

Figure 11. Static test setup.

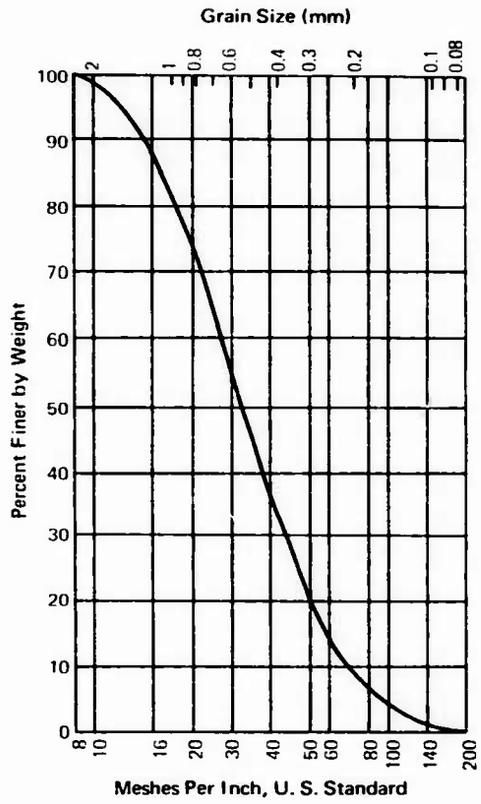

Figure 12. Grain size distribution of test sand.

Dynamic Tests. Stress cell SFB-1 was subjected to nine tests in the NCEL blast simulator (Figure 13) during the preliminary evaluation.[1] A description of the blast simulator is presented in Reference 7. A 10-foot-long, 3/8-inch-wall, 8-inch-diameter steel pipe, filled with the same dry-riverbed sand used in the static tests, was employed for these tests. Because of the pipe dimensions, sand density could not be controlled by dropping sand into the pipe over a specified height, as in the static tests. Instead, sand density was controlled by tapping along the length of the pipe with a sledge hammer, after the pipe was filled with sand, until no further settlement of the sand near the top was noted. The stress cell was placed 5-1/2 inches below the top of the pipe, with its **Z**-strain gage coincident with the axis of the pipe. Only the **X**-, **Y**-, and **Z**-strain gages inside the stress cell were monitored, because the loading on the sand column was axisymmetric. A greased, thin polyethylene liner was placed inside the upper section of the pipe to reduce attenuation of the applied dynamic pressure from wall friction. The 24-inch-long polyethylene liner and the upper 24 inches of sand at the top of the pipe were removed and replaced after each test. Moreover, a 1/8-inch-thick rubber membrane was placed on the top of the 8-inch-diameter pipe before the pipe was bolted to the flange on the blast simulator. This membrane prevented dynamic air pressure from entering into the pores between the sand grains. A pressure transducer, placed near the top of the pipe (see Figure 13) was used to measure dynamic pressures on the sand column. The peak pressure applied in these tests was about 105 psi.

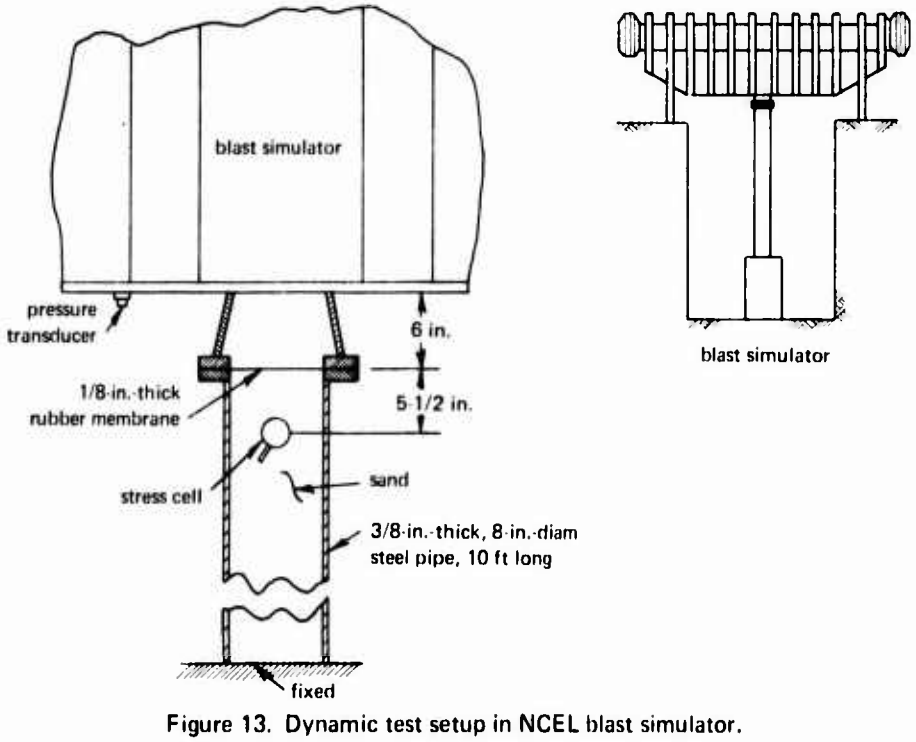

Figure 13. Dynamic test setup in NCEL blast simulator.

Stress cells SFB-3 and SFB-4 were subjected to three high-explosive tests on the beach at Point Mugu. A cross section of the test setup is shown in Figure 14. The 3-foot-long by 3-foot-OD (outside diameter) steel cylinder with 3/4-inch-thick wall was used as the pressure vessel. After the installation of the cylinder, sand directly under the cylinder was removed to a depth of about 2 feet below the bottom of the cylinder and replaced with dry beach sand. Two pressure transducers, placed with their active faces even with the sand surface inside the cylinder, were used to measure dynamic pressures on the sand surface. The two stress cells were placed at about 1 foot below the sand surface inside the tank as shown in Figure 14. A 40-inch-square by 5-1/8-inch thick wooden box filled with beach sand was placed on the top of the steel cylinder. This box was covered with a 2-foot-thick surcharge of beach sand to control the duration of the dynamic pressure pulse. Dynamic pressures were generated by exploding an 8-inch-diameter by 1/2-inch-thick charge of C-4 plastic explosive suspended in the center of the cavity inside the pressure vessel. Predicted peak dynamic pressure for the explosive charge used was 500 psi. The water table was located at about 5 feet below the level of the two stress cells.

The sand inside the tank was removed with a hand scoop to a depth of about 6 inches below the level of the stress cells and put back into place after each test. The stress cells were removed and reinstalled during this process. Special care was taken in compacting the sand around the stress cell during installation. The dry beach sand, however, because of its gradation, cannot be compacted densely.

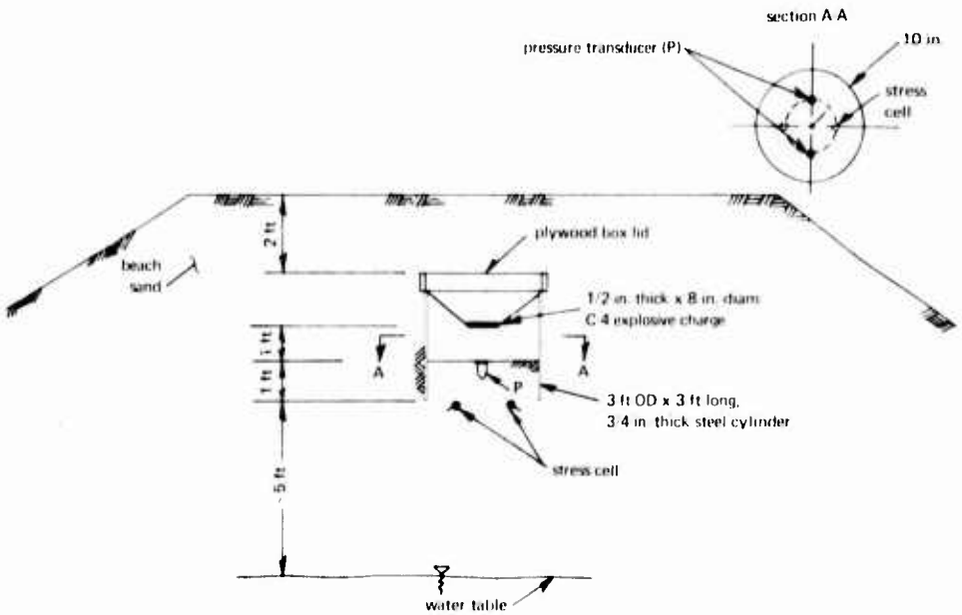

Figure 14. Dynamic test setup at Point Mugu.

Instrumentation

All the data from the hydrostatic tests and the static tests were recorded with a B&F SY256 data recording unit. The output is automatically digitized and printed on paper tape. Sand displacement in the static tests was measured with a Bourns 108 linear potentiometer that has a 6-inch travel.

In the dynamic tests performed in the NCEL blast simulator, pressures were measured with a Dynisco PTV6-3C pressure transducer. The resulting data from these dynamic tests were recorded directly with a CEC 5-124 oscillograph using a 600-Hz galvanometer.

Dynamic pressures from the tests at Point Mugu were measured with two Bytrex HFG-1000 pressure transducers. Data from these tests at Point Mugu were recorded on magnetic tape at a speed of 60 ips with a Sangamo 3562 tape recorder. The tape, after each test, was played back at 3-3/4 ips, through a CEC 5-124 oscillograph using a 5-kHz galvanometer. A time scale expansion of 16 was obtained on playback. The FM multiplexing unit that can transmit six channels of data information via one channel was not used in these tests because the special equipment required for reducing the data from the unit was not available.

RESULTS AND DISCUSSION

Hydrostatic Tests

The primary purpose of the hydrostatic tests was to check whether all of the embedded strain gages in the stress cell were functioning. These tests were not used for calibration purposes, no calibration of the stress cell is required. The strain data from different stress cells were nearly identical. Furthermore, there is very little difference in data obtained for the three loading cycles. A plot of typical strain data from the three strain rosettes is presented in Figure 15. As can be seen, the response of the embedded strain gages is linear to 3,000 psi. Also, the slopes of the three curves in Figure 15 are essentially identical, indicating that there is very little difference in behavior among the three strain rosettes.

The average bulk modulus, computed from the hydrostatic stress cell data, was 0.933×10^6 psi. The corresponding value computed by using the modulus of elasticity and Poisson's ratio for the cue ball was 0.950×10^6 psi. Thus, the strain distribution within the stress cell remains essentially unchanged by the presence of the embedded strain gages and the handle.

Static Tests

General. A typical consolidation curve for the sand used in the static tests is presented in Figure 16. It can be seen from this figure that the amount of consolidation per unit load increment decreases with increasing load for all three cycles and approaches an almost constant value for applied loads of greater than 300 psi. The sand had a permanent set at the end of each cycle after the load was removed; this permanent set increased slightly with each succeeding load cycle. Moreover, the sand crept at maximum load (Figure 16) when the load was held constant for 3 minutes. A plot of the tangent moduli of the sand during loading is given in Figure 17. In the first cycle, the tangent modulus of the sand increased from an initial value of about 7,000 psi at zero load to a value of about 30,000 psi at maximum applied load—an increase of about four times the initial value. In the second and third cycles, the tangent modulus of the sand increased from an initial value of about 14,000 psi at zero load to maximum values of about 82,000 psi and 105,000 psi, respectively, at 660 psi and 770 psi. Thereafter, the tangent modulus of the sand decreased with increasing load. In general, the tangent modulus of the test sand varied considerably with the magnitude of the applied load and its loading history.

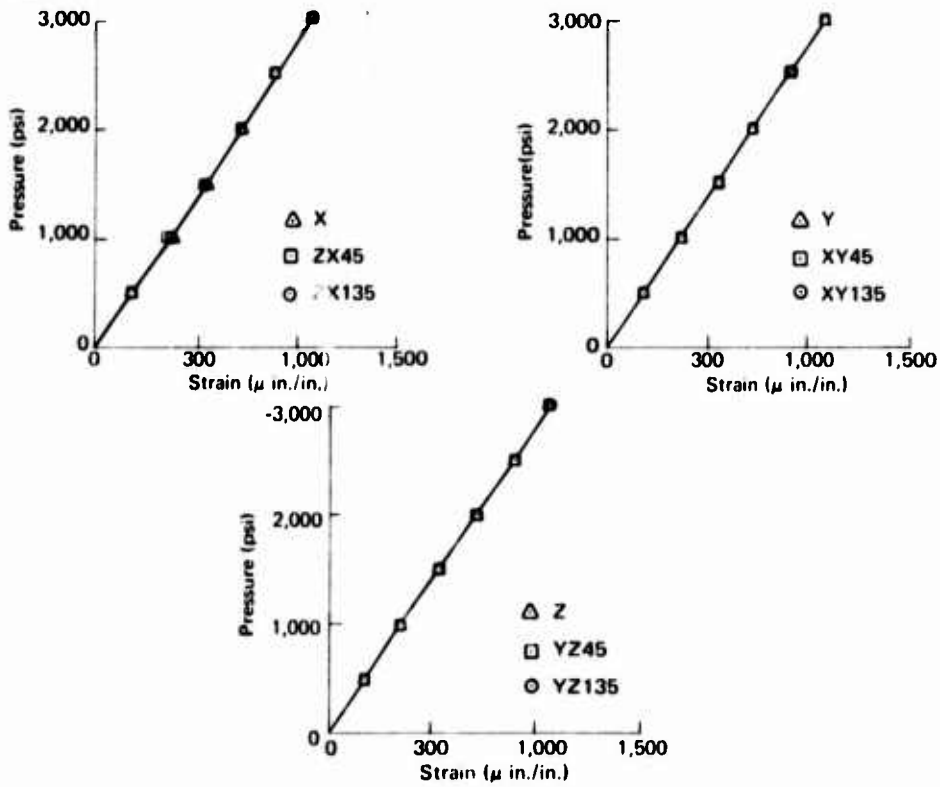

Figure 15. Typical hydrostatic data from stress cell.

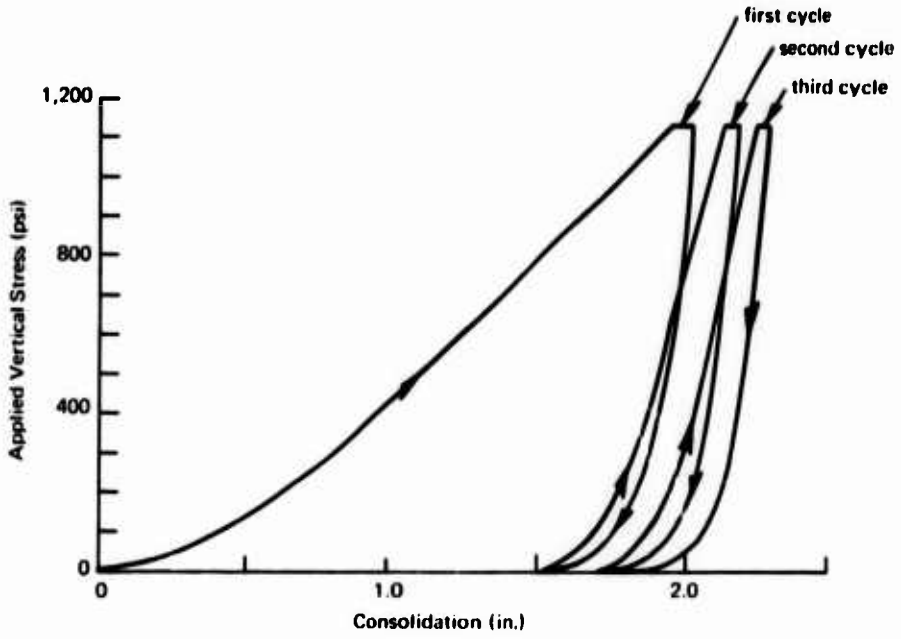

Figure 16. Load versus sand consolidation, static tests.

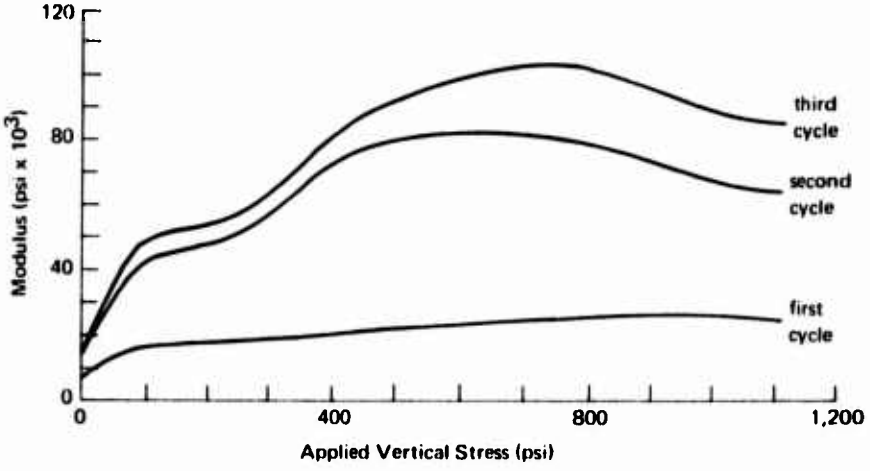

Figure 17. Tangent modulus of sand, static tests.

Typical strain data from the stress cell for the static normal tests are presented in Figure 18. Strain data from the **X**- and **Z**-strain gages are presented in this figure. The data from the **Y**-strain gage are not presented because they are similar to those from the **X**-strain gage. Strain data from the **Z**-strain gage and the **X**-strain gage tended to concave upward slightly with increasing applied load during the first cycle. On the other hand, data from the **Z**-strain gage and **X**-strain gage increased linearly with load for applied loads greater than 100 psi during the second and third cycles. During unloading, as indicated by the dotted lines in Figure 18, the data for the three cycles from a given strain gage in the stress cell followed essentially the same path. Furthermore, trends similar to those mentioned above for the static normal test data from the stress cell were present in the data from the shear tests.

A significant point not apparent from the data presented in Figure 18, is that, while under maximum load, the sand underwent creep (Figure 16) but the stress cell did not, which indicated that the response of the stress cell is insensitive to creep in the soil.

The direct–normal, lateral–normal, and shear stress influence coefficients used in the reduction of the static data from the stress cells, were 0.572, 0.043, and 0.529, respectively. These coefficients corresponded to a modular ratio $\mathbf{E_c/E_h}$ of 10 and a Poisson's ratio ν_c/ν_h of 1.0 in Figures 5, 6, and 7.

Tests for Normal Stress Response. The objective of the static normal test is to determine the accuracy of the normal stress measurements obtained from the stress cell in sand. Normal stresses, vertical and horizontal, were computed from the stress cell data using Equations 1 through 3 and 10 through 12. The applied vertical stress was used to compare the vertical stress from the stress cell, for lack of a better standard. At the level of the stress cell (see Figure 11), the actual vertical stress, will understandably be somewhat smaller than the applied stress on top of the tank because of wall friction. Average lateral stresses in the sand at the level of the stress cell, computed from the soil tank strain data, were compared with the corresponding lateral stresses from the stress cell. These lateral stresses from the soil tank data are not sensitive to friction between the liner and tank wall because they are computed from local measurements. Unfortunately, vertical strains from the soil tank wall adjacent to the stress cell, because of their relatively small magnitudes, cannot be used in computing the vertical stresses in the tank wall. Hence, no quantitative estimate of the decrease in the applied vertical load from wall friction at the level of the stress cell was made.

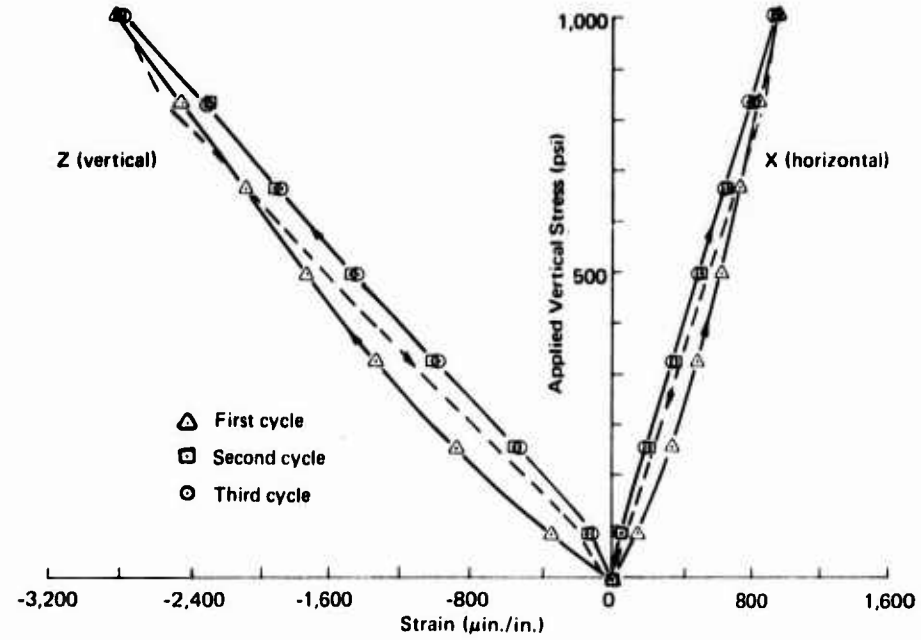

Figure 18. Typical stress cell data, static normal tests.

Comparisons of vertical stress from the stress cells with the applied vertical stress are presented in Figures 19 through 26. In these figures, the stress from the stress cells is expressed as a percentage of the corresponding applied vertical stress. Unloading is represented by the dotted lines. It is apparent that during the first cycle the vertical stress from the stress cell approaches the applied stress from the high side as the applied load increases. This phenomenon is caused by the larger vertical displacement of the sand near the tank wall, because of its proximity to the greased plastic liner, relative to the vertical displacement of the sand near the center of the tank. The greased liner offered less restraint to vertical displacement of the sand particles than did the sand particles themselves. This relative vertical displacement causes more applied load to be carried by the sand near the center of the tank than by the sand near the tank wall; hence, the high response of the stress cell.

As the applied load is increased, and the sand is compacted, the relative vertical displacement between the sand particles near the center of the tank and those near the tank wall becomes less and less. As a consequence, vertical stress from the stress cell approaches the applied stress as the applied stress increases. It is also apparent from Figures 19 through 26 that the response curves of the stress cell during the second and third cycles are very close together despite the changes in the tangent moduli of the sand from the second to the third load cycle (Figure 17). The vertical stress from the stress cell during the second and third cycles, which is initially smaller than the applied stress, approaches the applied stress as the applied load increases.

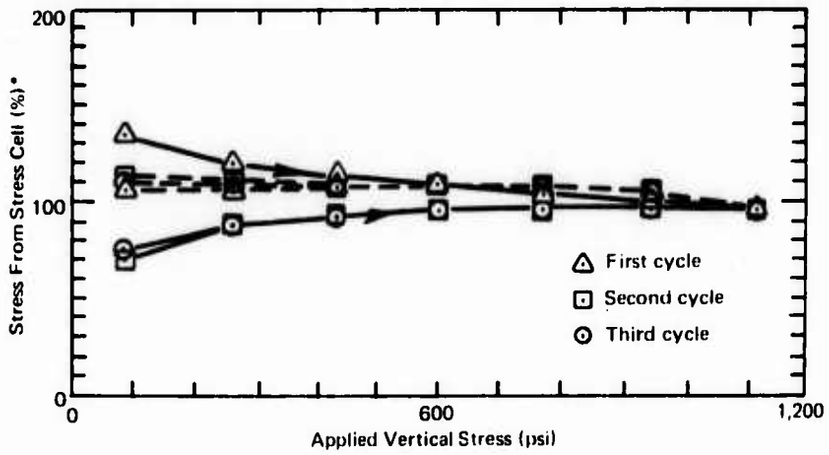

*Percent of applied vertical stress.

Figure 19. Comparison of vertical stresses, static normal test 1, SFB-3.

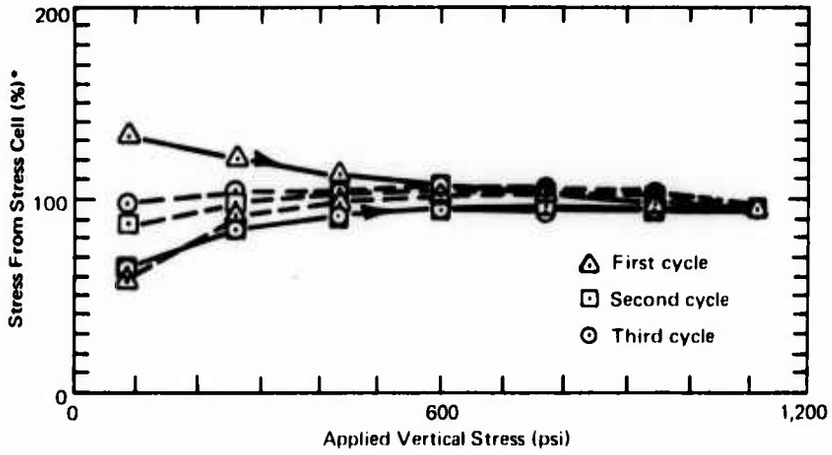

*Percent of applied vertical stress.

Figure 20. Comparison of vertical stresses, static normal test 2, SFB-2.

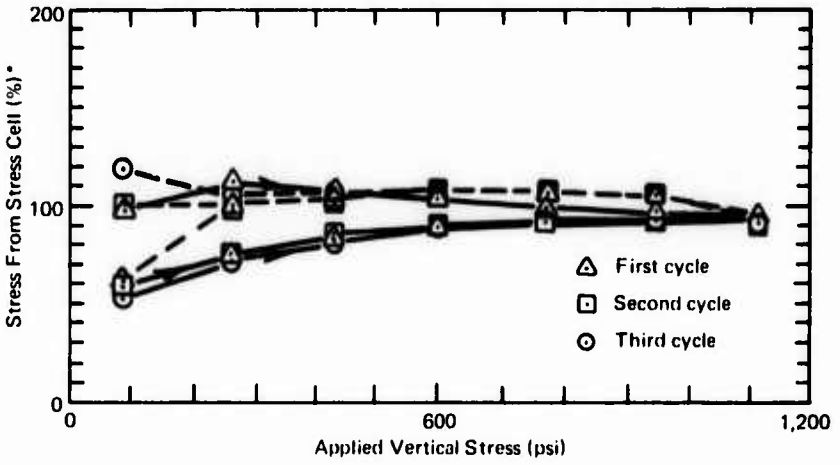

*Percent of applied vertical stress.

Figure 21. Comparison of vertical stresses, static normal test 3, SFB-4.

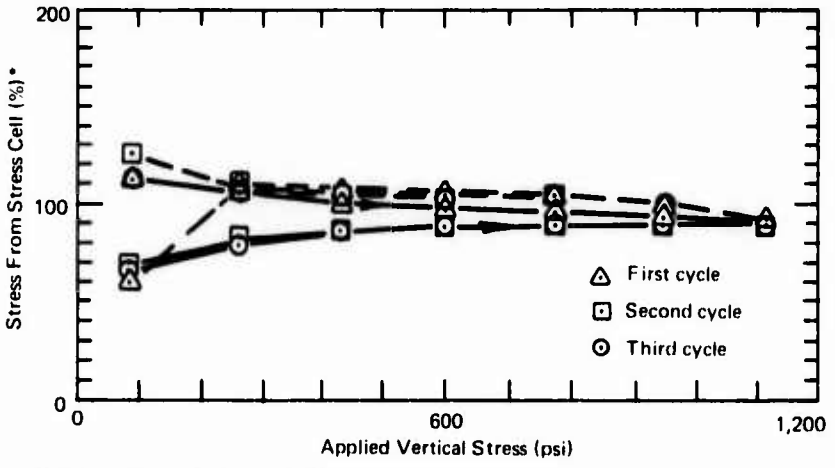

*Percent of applied vertical stress.

Figure 22. Comparison of vertical stresses, static normal test 4, SFB-5.

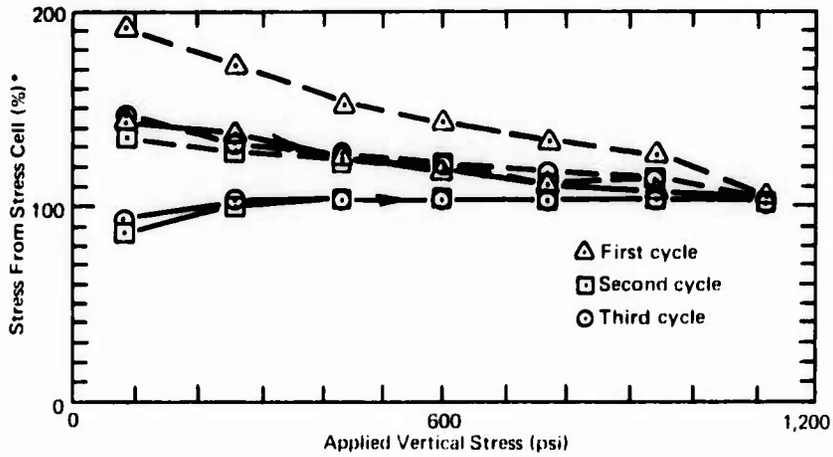

*Percent of applied vertical stress.

Figure 23. Comparison of vertical stresses, static normal test 5, SFB-5.

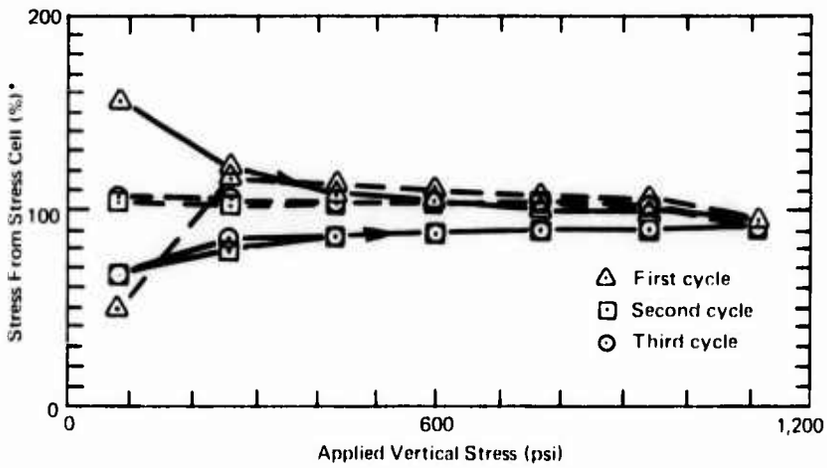

*Percent of applied vertical stress.

Figure 24. Comparison of vertical stresses, static normal test 6, SFB-3.

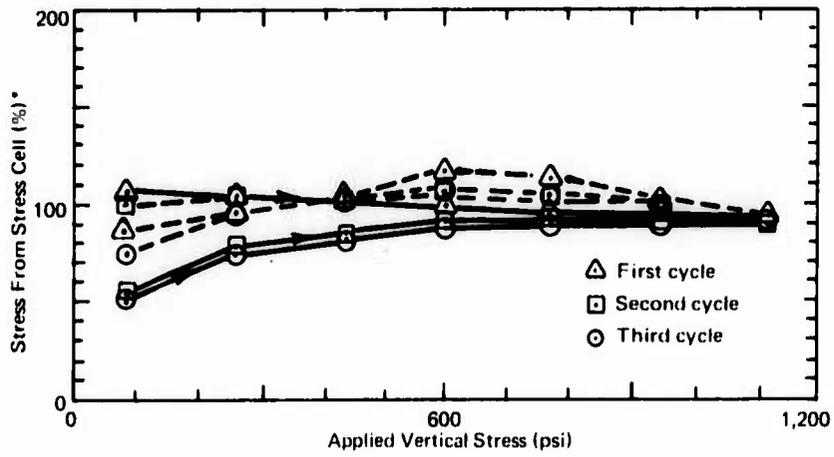

*Percent of applied vertical stress.

Figure 25. Comparison of vertical stresses, static normal test 7, SFB-2.

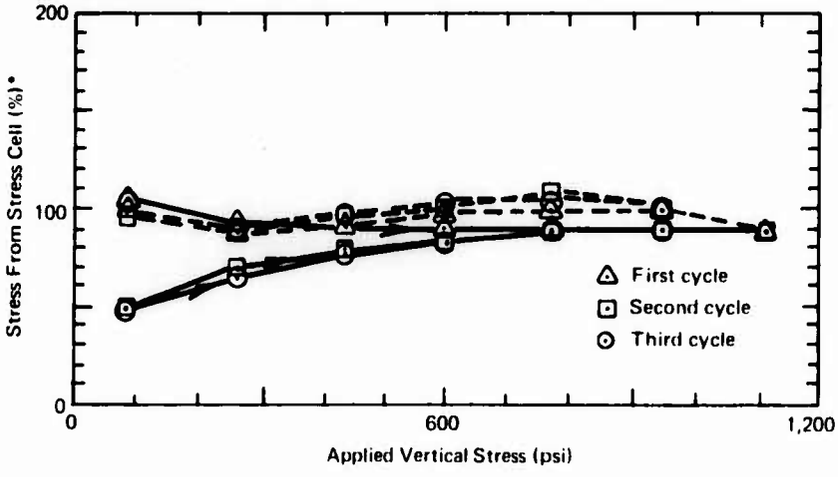

*Percent of applied vertical stress.

Figure 26. Comparison of vertical stresses, static normal test 8, SFB-4.

For applied loads equal to or greater than 600 psi, the vertical stresses from the stress cells are within ±10% of the corresponding applied vertical stresses. With a few exceptions, especially test 5 (Figure 23), the vertical stress from the stress cell during unloading (dotted lines in Figures 19 through 26) is about 10% larger than the corresponding applied stress for all three cycles. This high response of the stress cell during unloading is caused by vertical residual stress in the sand. Another point is that the unloading paths in Figures 19 through 26 are generally closely banded together with the band widening for loads below 300 psi. In short, the vertical stress from the stress cell approaches the applied stress with increasing load from the high side during the first cycle and from the low side during the second and third cycles. Vertical stress from the stress cell is within ±10% of the applied stress for applied stresses equal to or greater than 600 psi. Next, lateral stresses from the stress cell are compared with those from the soil tank.

Comparisons of lateral stresses from the stress cells with those from the soil tank are presented in Figures 27 through 34. In these figures, the lateral stresses are plotted against the applied vertical stresses. Lateral stresses from the stress cell were computed by averaging the stresses in the **X**- and **Y**-direction (Figure 11); those from the soil tank were computed by averaging the lateral stresses from the four pairs of strain gages on the soil tank wall. From Figures 27 through 34, it is apparent that lateral stresses from the stress cell are generally smaller than those from the soil tank during the first cycle loading—a phenomenon caused by the presence of the greased plastic liner. The presence of the greased plastic liner evidently caused relative vertical displacement within the sand that induced more load through the sand near the middle of the soil tank where the stress cell was located. This difference in load created a void ratio gradient in the sand that increased with increasing radial distance from the axis of the soil tank. Because the at-rest coefficient of earth pressure, K_o (the ratio between the horizontal and the vertical stress) is proportional to the void ratio, the low void ratio of the sand near the center of the tank relative to the sand near the tank wall brought about the smaller lateral stresses from the stress cell. This difference in lateral stresses becomes less with succeeding load cycles as the sand becomes more compacted.

Agreement between the lateral stress from the stress cell and that from the soil tank during loading is generally within ±10%. During unloading, the lateral stress from the stress cell is slightly larger than its corresponding

stress during loading for all three cycles. By contrast, lateral stress from the soil tank during unloading is generally much larger than its corresponding stress during loading. This larger lateral stress from the soil tank during unloading must have been caused by the residual stress in the sand, because no additional lateral stress was applied. Apparently, during unloading, the sand particles locked into rings symmetrical about the axis of the tank. The sand in the 17-inch-diameter tank can be visualized as seventeen 1-inch-thick (measured radially) concentric rings. The rings near the tank wall, because of their larger radius, unloaded much more slowly than those near the stress cell; hence, the larger lateral stress from the soil tank during unloading. The lateral stress from the stress cell and that from the soil tank, with a few exceptions, are within ± 10% of each other, even for an applied vertical stress of less than 600 psi.

In 1963, Hendron[8] performed a series of experiments to study the behavior of sand in one-dimensional compression. He concluded that a straight-line relationship exists between horizontal and vertical stresses for applied stresses up to about 1,000 psi. Hendron reported that the value of K_o depends upon the type of sand and its initial void ratio. The response of the stress cell to applied normal stresses is presented in Figures 35 through 42. As with Hendron's results, the relationship between the horizontal and vertical stresses is linear for loading and unloading. For each test, K_o (the slope of the curve) decreases with each succeeding load cycle as the void ratio of the sand becomes smaller. The lateral stress coefficients, K_o, from these tests varied between 0.34 and 0.44. The average value was 0.40. Corresponding K_o values obtained from previous experiments at NCEL[9] using the same sand varied between 0.41 to 0.45.

The vertical response of the stress cell (Figures '9 through 26) for applied loads of less than 600 psi is also within 10% absolute of the corresponding applied value. The relationship between the horizontal and vertical stresses from the stress cell is linear throughout the loading range for all of the tests. It is in good agreement with corresponding values obtained for the same sand in previous experiments. Consequently, the accuracy of the vertical stress measurements obtained from the stress cell for applied loads less than 600 psi is as accurate as its lateral response. Likewise, the accuracy of the lateral stress measurements from the stress cell for applied vertical loads greater than 600 psi is as accurate as its vertical response. As a result, the horizontal and vertical response of the stress cell to normal stresses is generally within 10% absolute of the applied value.

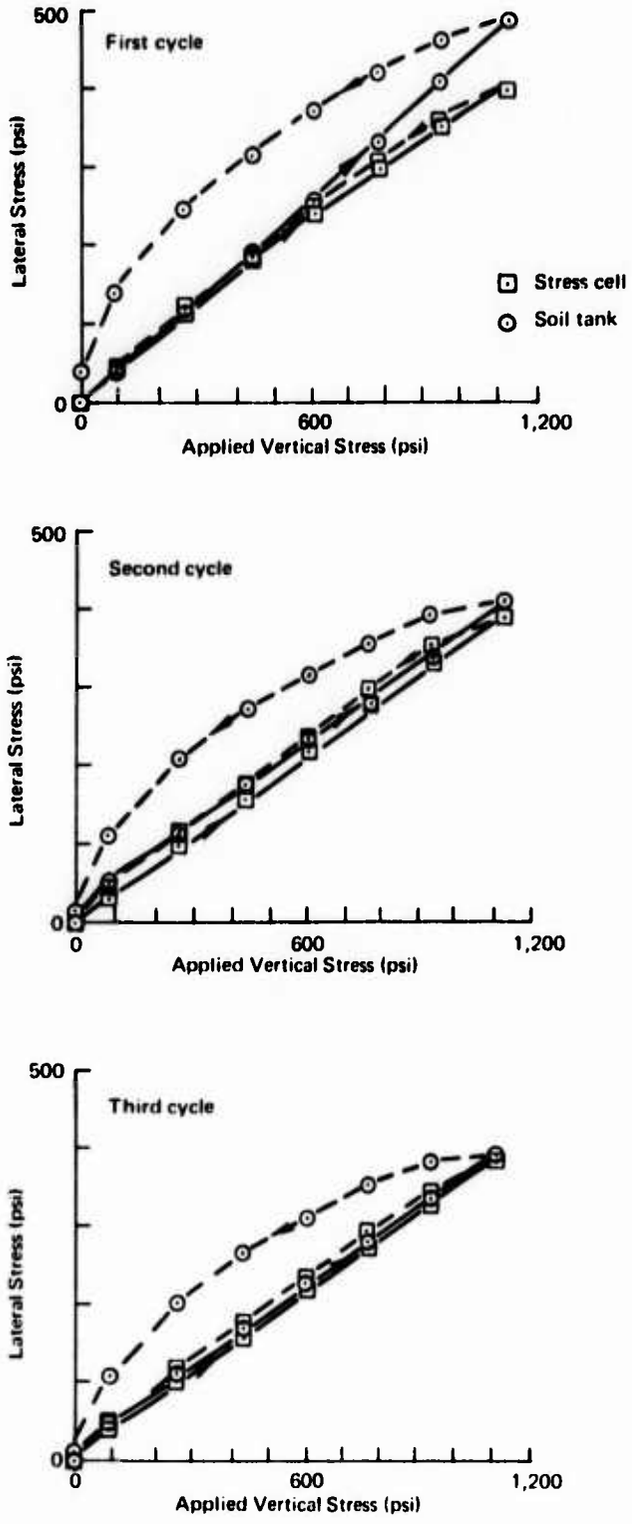

Figure 27. Comparison of lateral stresses, static normal test 1, SFB-3.

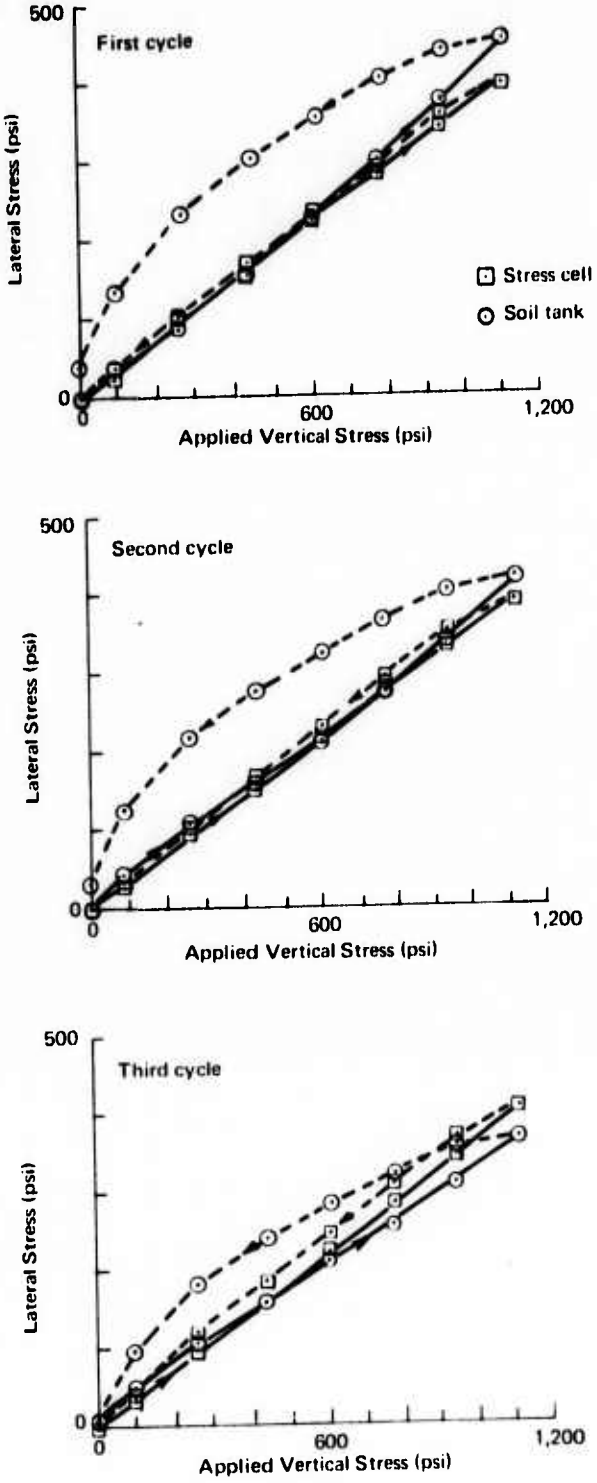

Figure 28. Comparison of lateral stresses, static normal test 2, SFB-2.

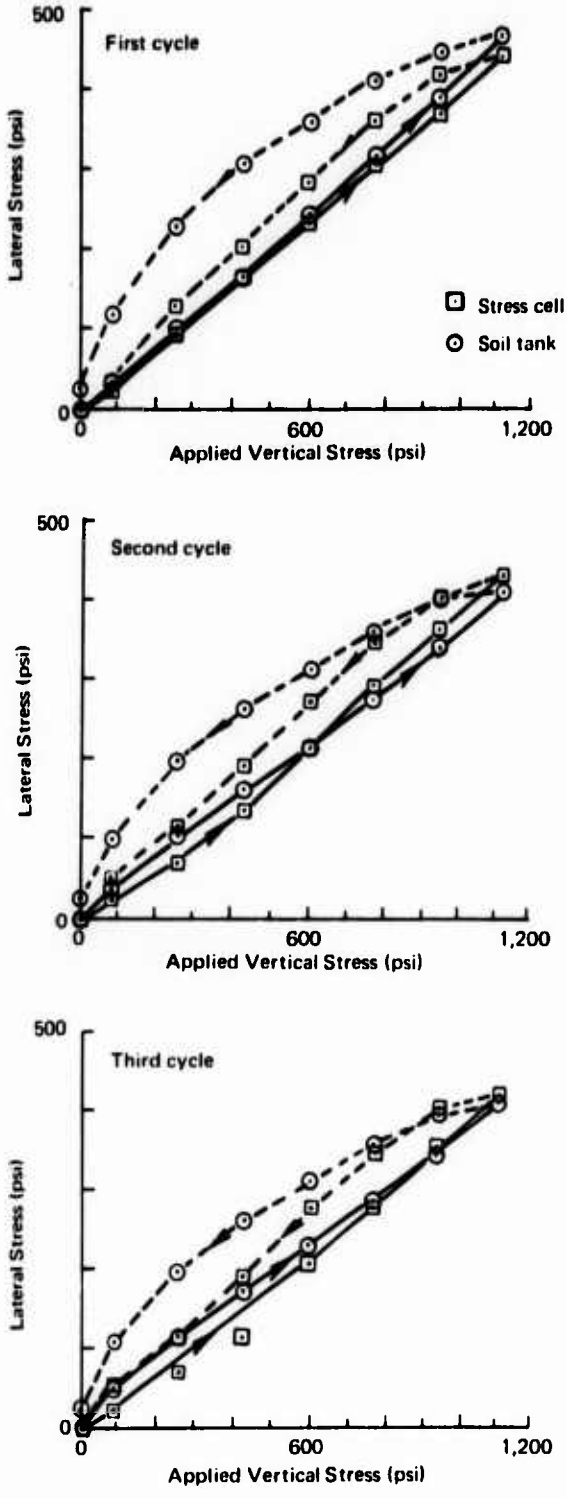

Figure 29. Comparison of lateral stresses, static normal test 3, SFB-4.

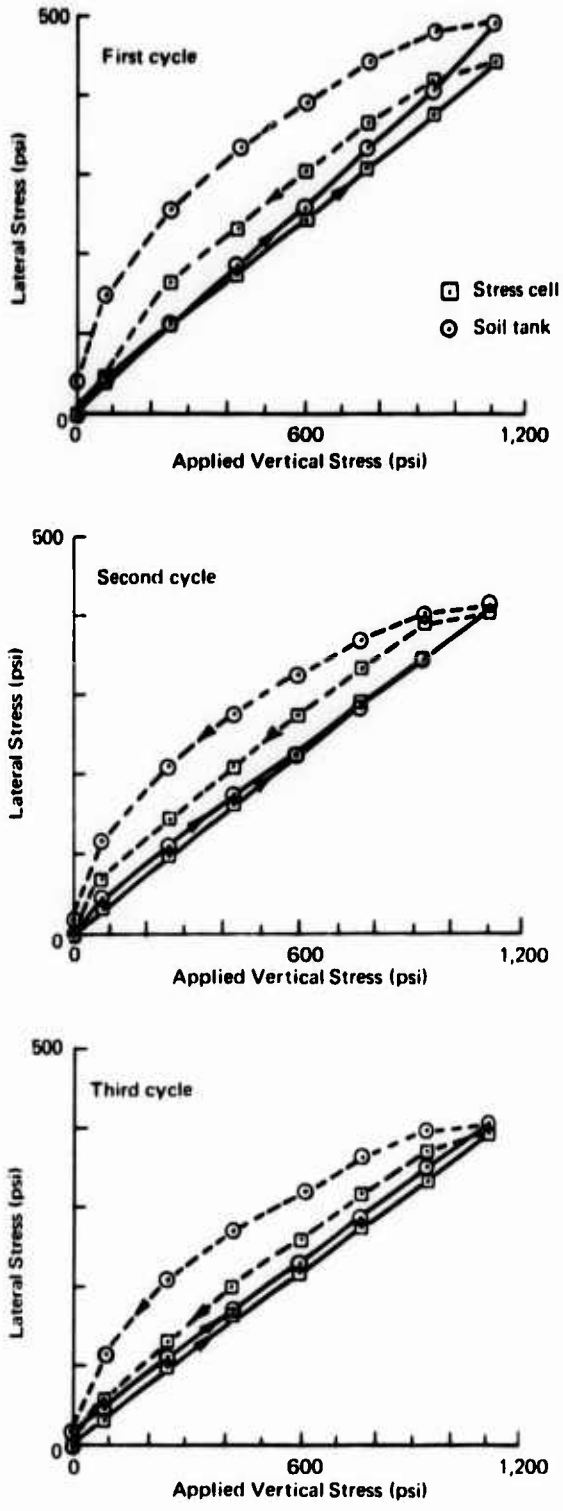

Figure 30. Comparison of lateral stresses, static normal test 4, SFB-5.

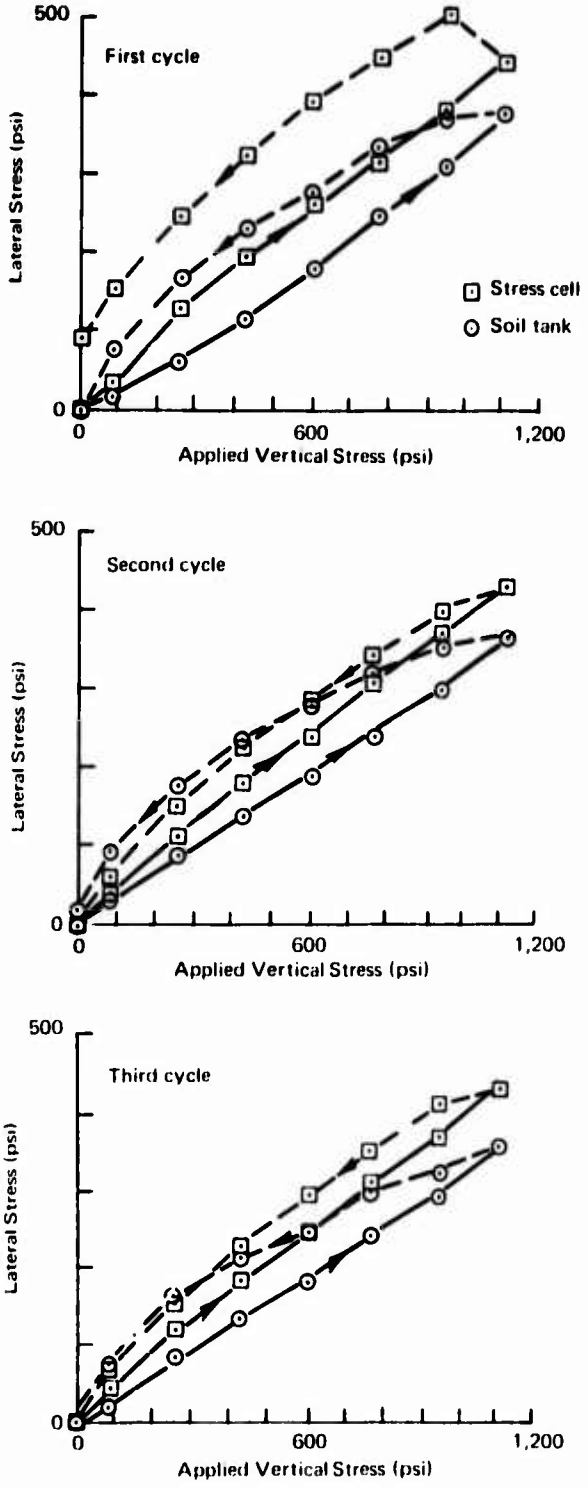

Figure 31. Comparison of lateral stresses, static normal test 5, SFB-5.

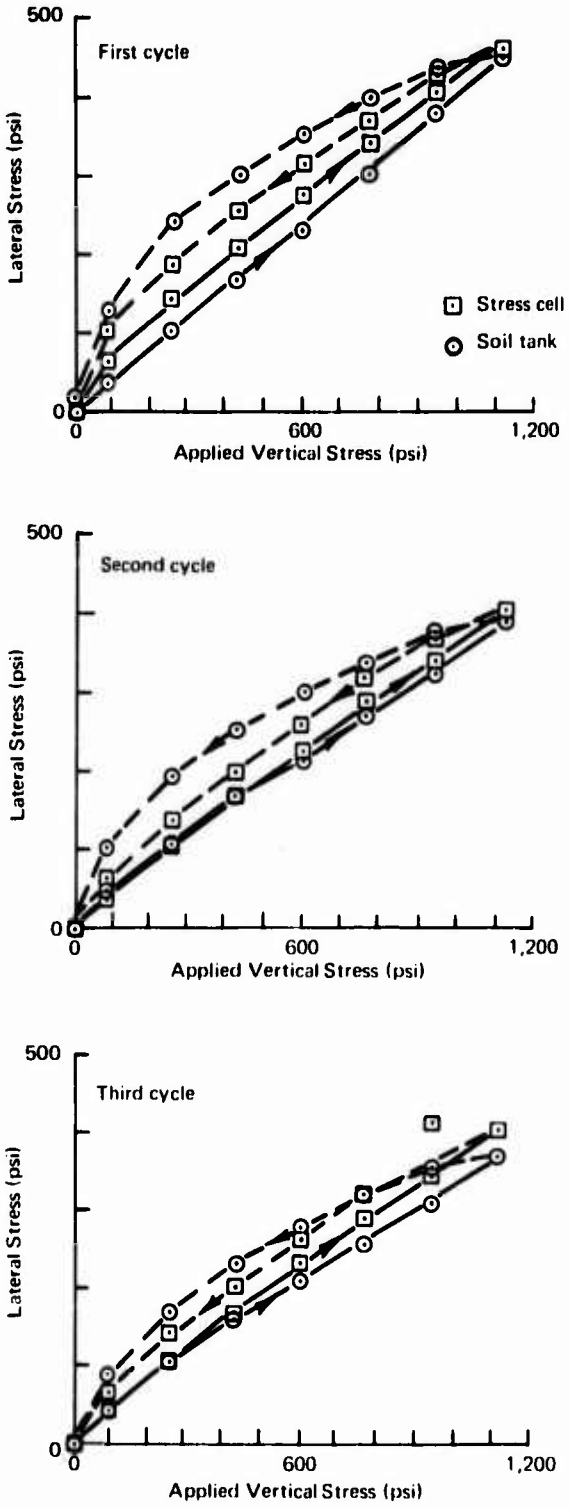

Figure 32. Comparison of lateral stresses, static normal test 6, SFB-3.

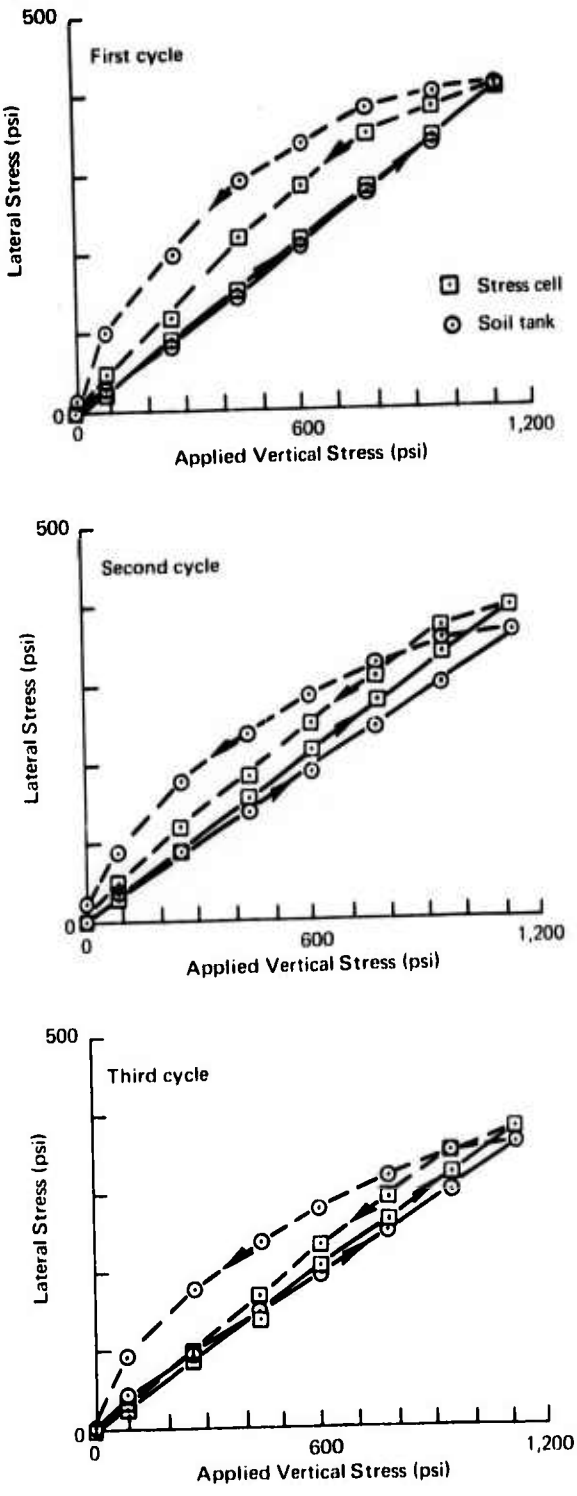

Figure 33. Comparison of lateral stresses, static normal test 7, SFB-2.

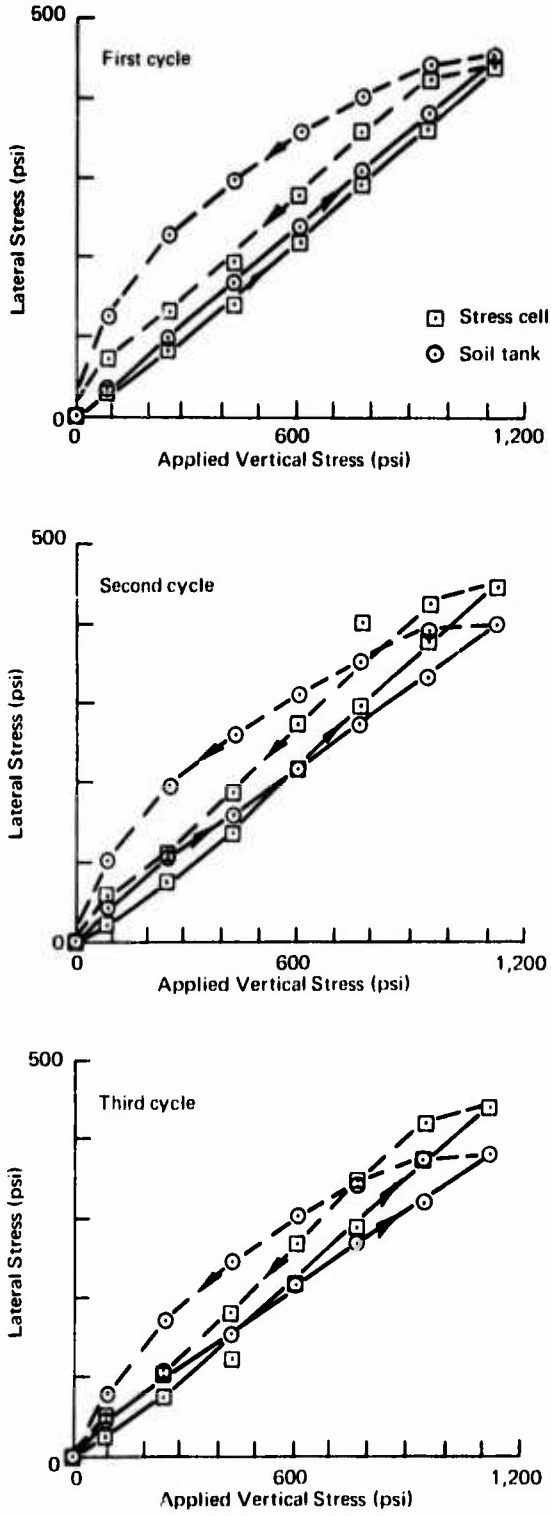

Figure 34. Comparison of lateral stresses, static normal test 8, SFB-4.

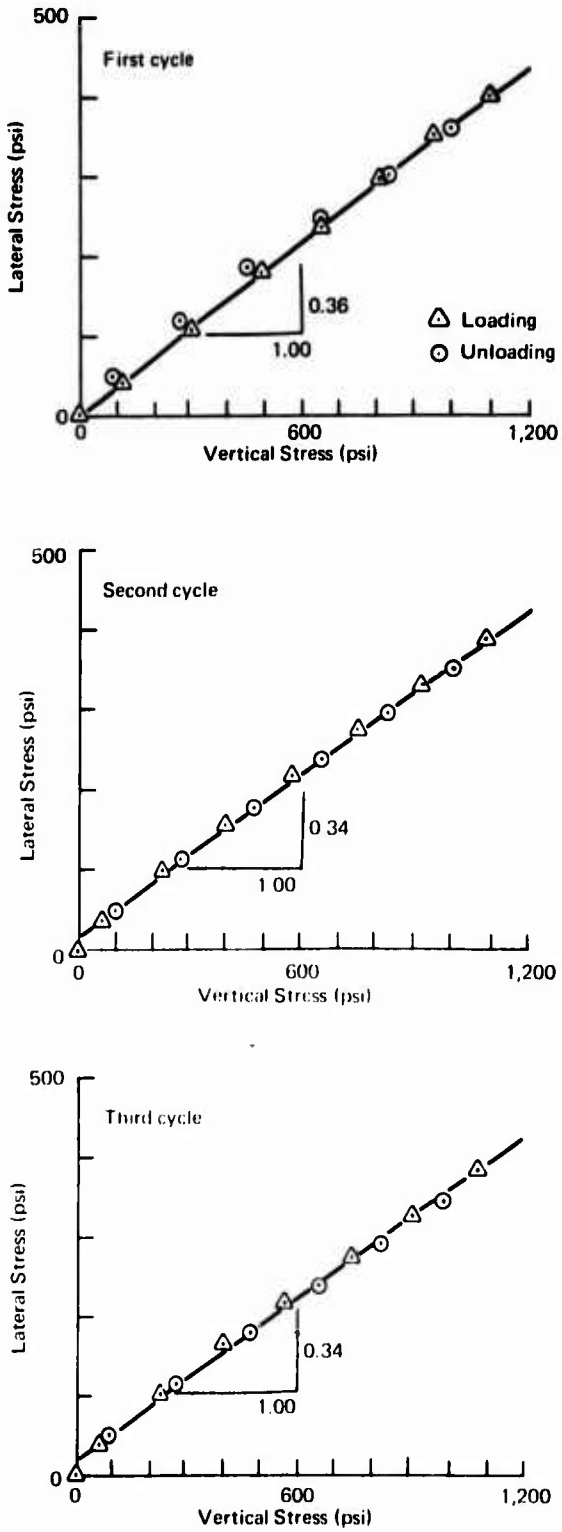

Figure 35. Vertical and horizontal stresses from stress cell, static normal test 1, SFB-3.

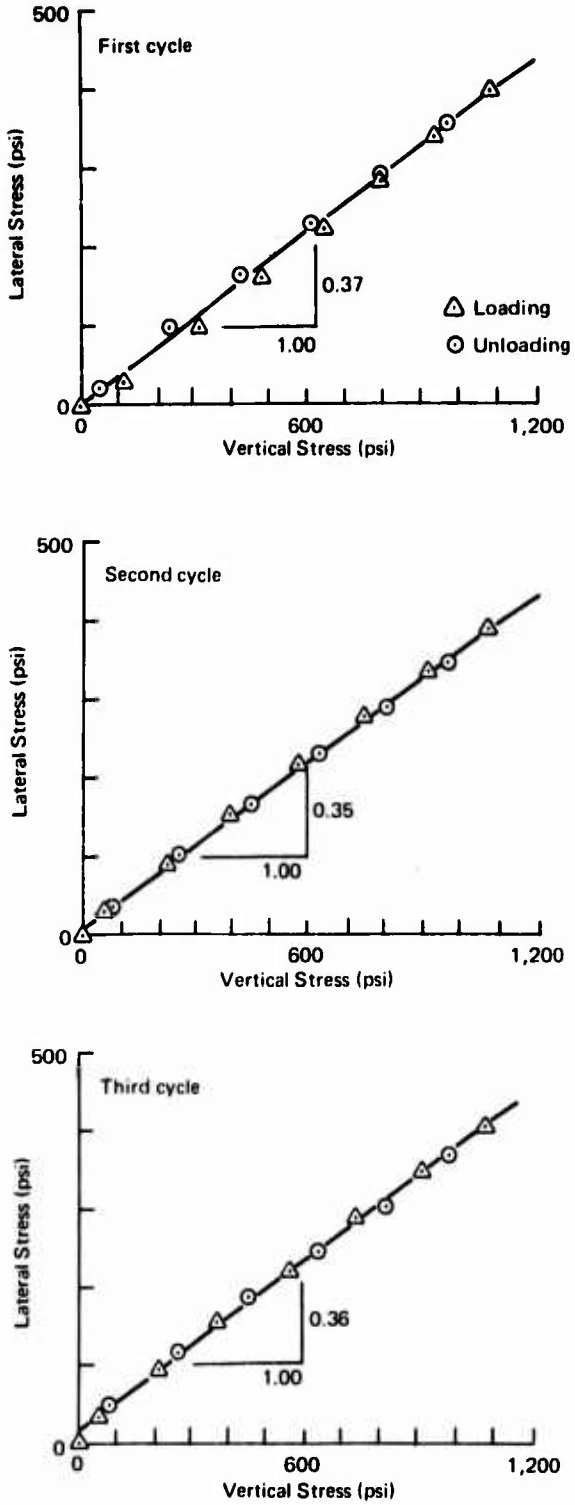

Figure 36. Vertical and horizontal stresses from stress cell, static normal test 2, SFB-2.

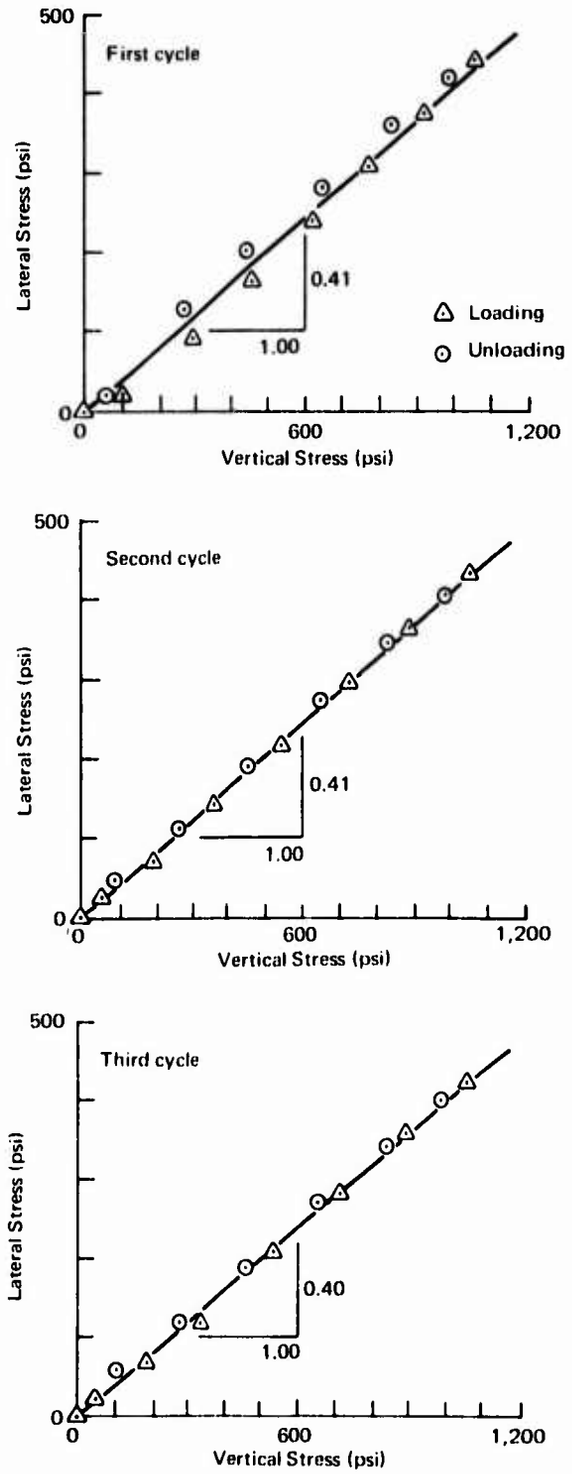

Figure 37. Vertical and horizontal stresses from stress cell, static normal test 3, SFB-4.

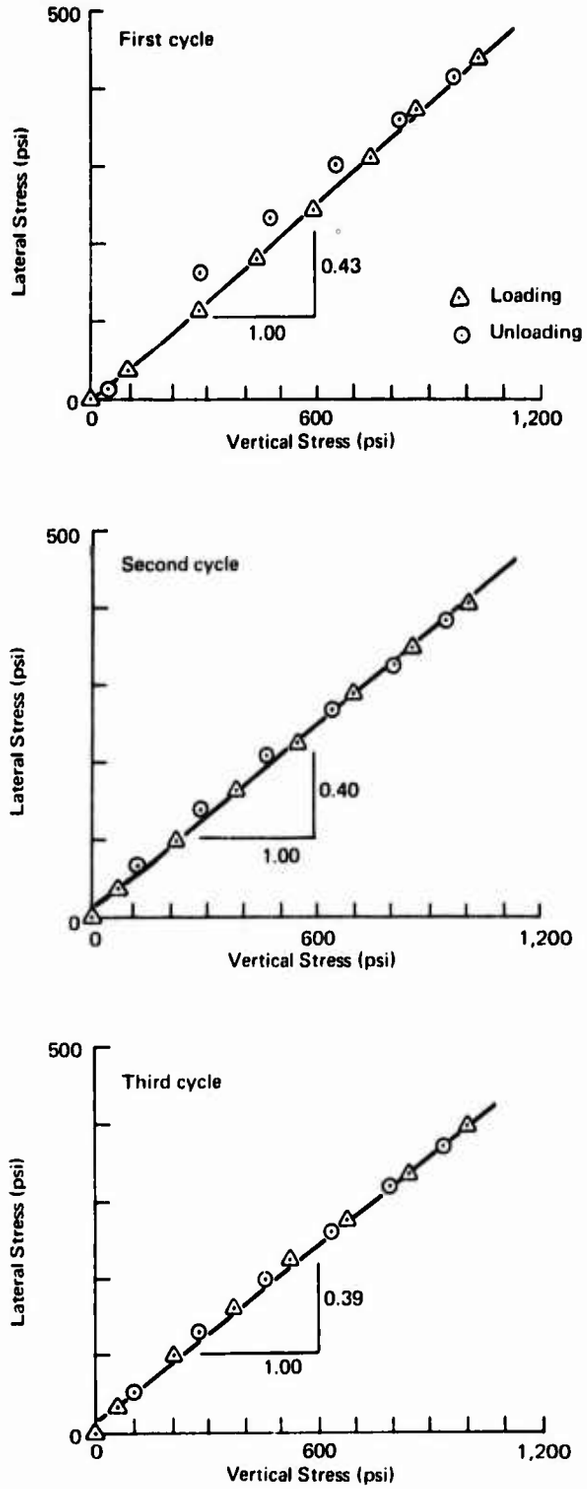

Figure 38. Vertical and horizontal stresses from stress cell, static normal test 4, SFB-5.

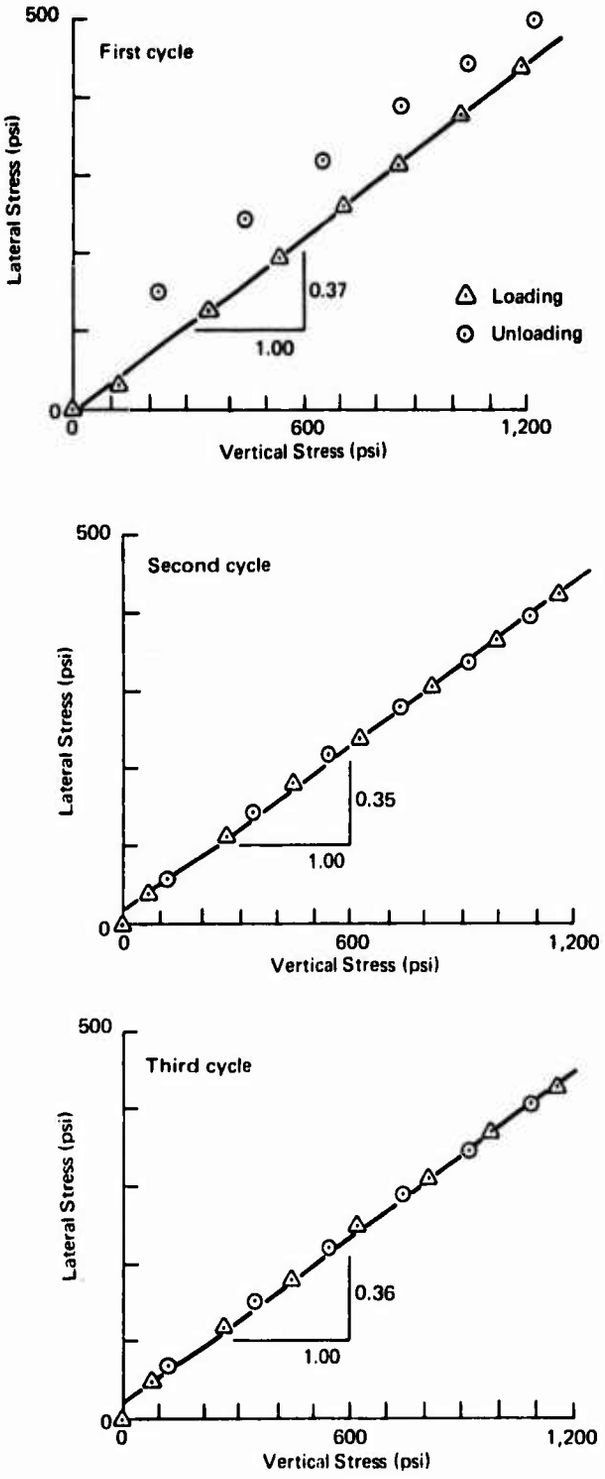

Figure 39. Vertical and horizontal stresses from stress cell, static normal test 5, SFB-3.

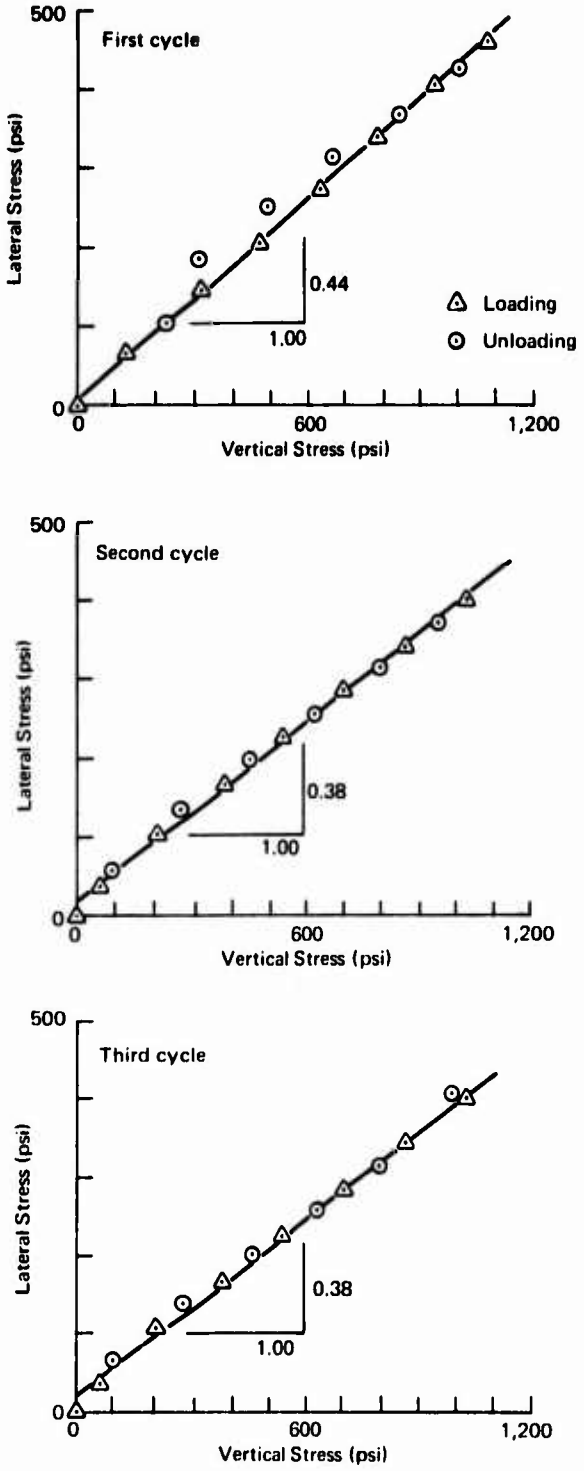

Figure 40. Vertical and horizontal stresses from stress cell, static normal test 6, SFB-3.

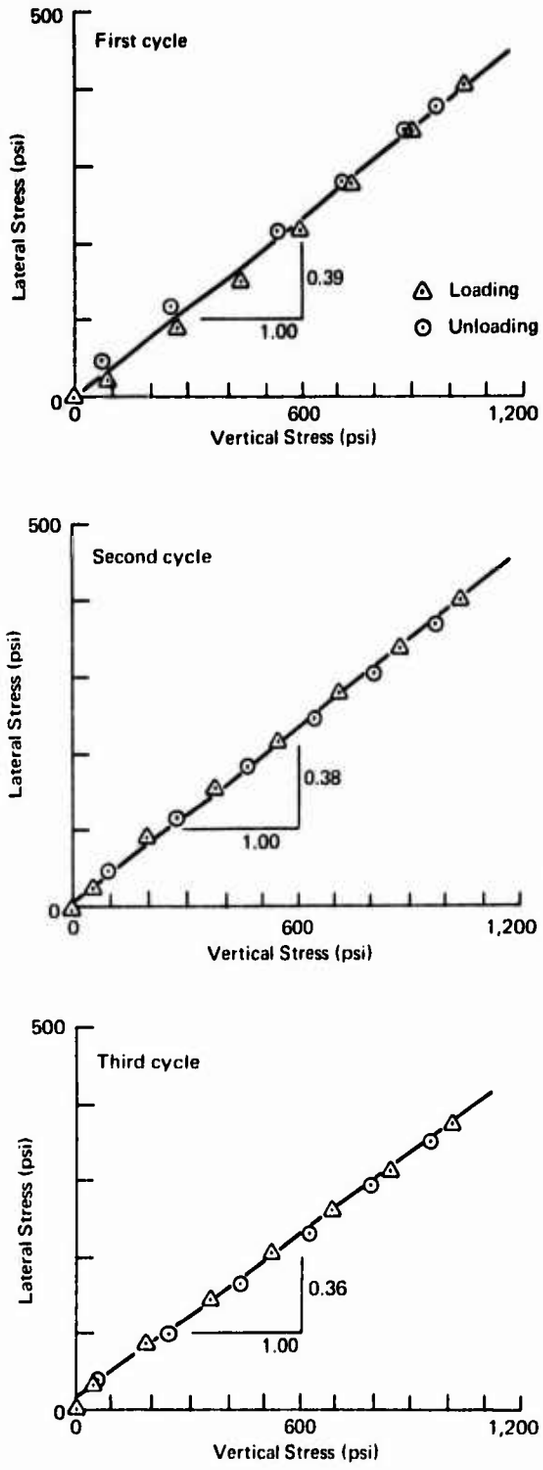

Figure 41. Vertical and horizontal stresses from stress cell, static normal test 7, SFB-2.

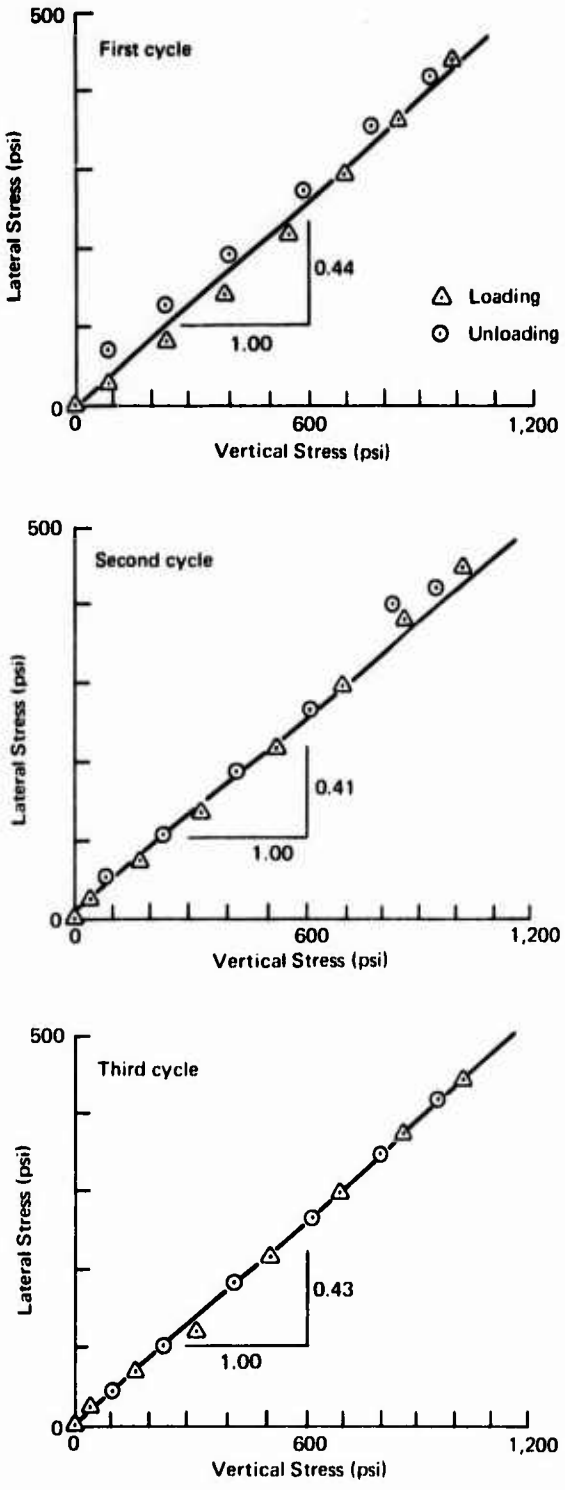

Figure 42. Vertical and horizontal stresses from stress cell, static normal test 8, SFB-4.

Shear Tests. Data from the shear tests were reduced by using Equations 1, 2, 3, 5, 10, 11, 12, and 19 with direct–normal, lateral–normal, and shear stress influence coefficients of 0.572, 0.043, and 0.529 from Figures 2 and 3. In addition, vertical stresses were computed from the stress cell data using the law of stress transformation.[10] Shear stresses from the stress cells were compared with the applied shear stresses computed by taking one half the difference between the applied vertical stress and the corresponding lateral stress from the soil tank. Understandably, the applied shear stress (designated) will be lower than the actual shear stress on the stress cell during loading in the first cycle because of the relative vertical displacement in the sand. Also, the applied shear stress during unloading will be lower than the actual shear stress on the stress cell as a result of the higher residual lateral stresses in the sand near the tank wall relative to those in the sand near the center of the soil tank. (See the discussion of the results from the static normal tests.)

Comparisons of shear stress from the stress cells with the corresponding applied shear stress are presented in Figures 43, 44, and 45. In these figures, shear stress from the stress cell is expressed as a percentage of the corresponding applied shear stress. The trends of the response to shear stresses during loading are similar to those in the comparison of vertical stresses in the static normal tests except during unloading. Shear stress from the stress cell approaches the corresponding applied shear stress from the high side as the applied load is increased during the first cycle. By contrast, the shear stress from the stress cell approaches the corresponding applied value from the low side as the applied load is increased during the second and third cycles. With the exception of the first cycle, the shear stresses from the stress cell are generally within 10% absolute of the applied shear stresses. The shear stresses from the stress cell during unloading for all three cycles were always larger than the applied shear stress (computed) because the lateral stress in the sand near the tank wall was larger than the corresponding stress near the center of the soil tank (see the discussion on the comparison of lateral stresses from the static normal tests). The applied shear stress was computed by taking one-half the difference between the applied vertical stress and the lateral stress from the soil tank. Thus, the applied shear stress during unloading was larger than the actual shear stress on the stress cell. In brief, shear stress from the stress cell is generally with ± 10% of the applied shear stress.

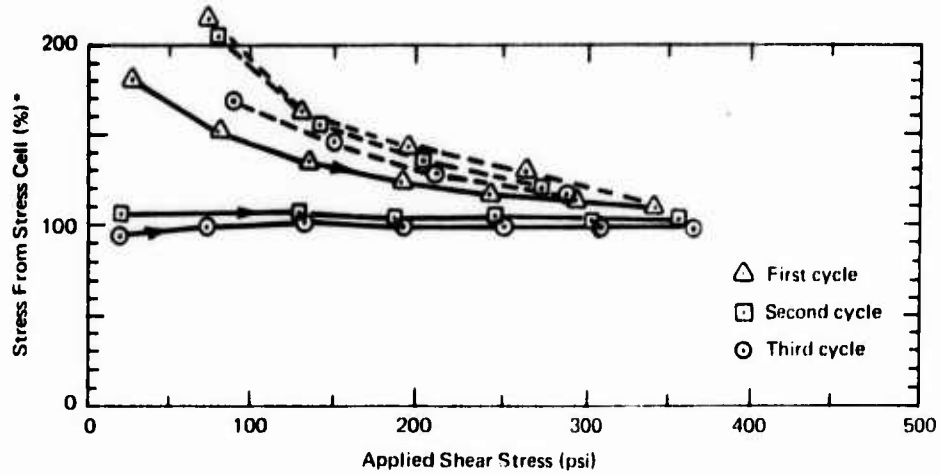

*Percent of applied shear stress.

Figure 43. Comparison of shear stresses, static shear test 1, SFB-4.

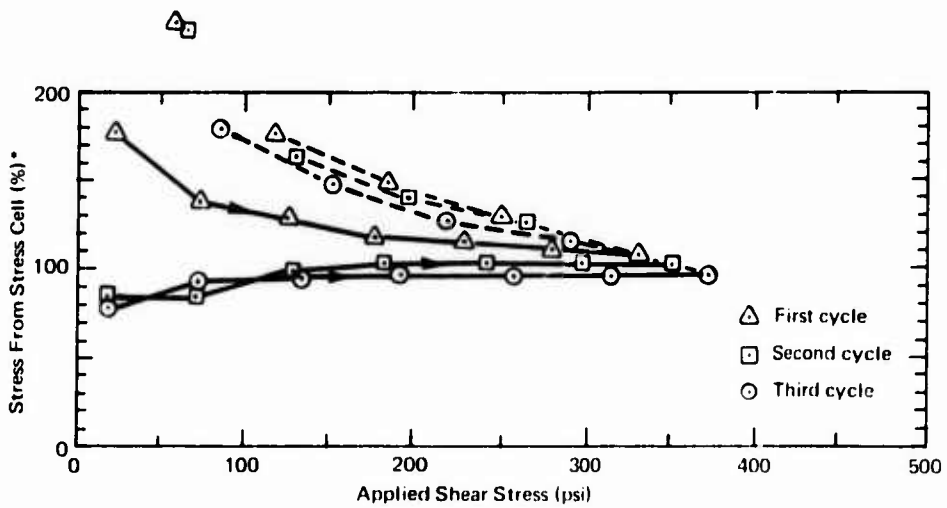

*Percent of applied shear stress.

Figure 44. Comparison of shear stresses, static shear test 2, SFB-5.

Vertical stresses from the stress cell, computed by transformation, were compared with the applied vertical stresses in the shear tests (Figures 46, 47 and 48) to verify whether the law of stress transformation can be applied to the stress measurements from the stress cell. Clearly, the trends and magnitudes shown in Figures 46, 47, and 48, and those shown in Figures 19 through 26 from the static normal tests are almost identical. Transformation, then, can be applied to stress measurements from the stress cell.

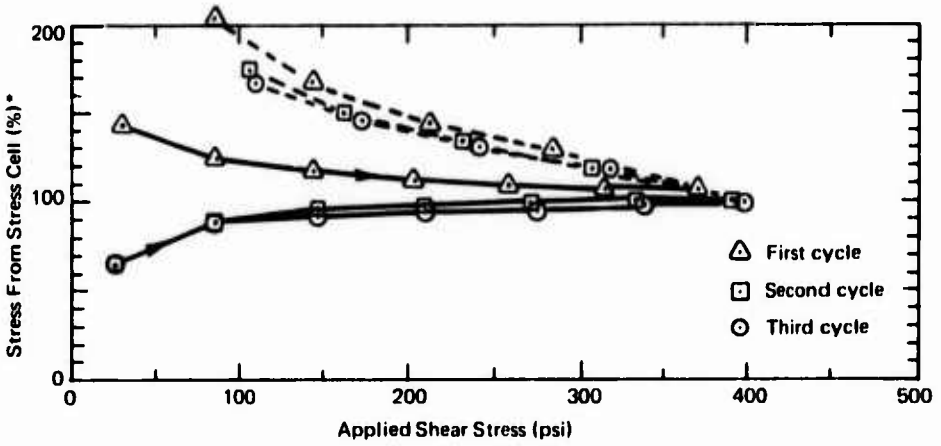

*Percent of applied shear stress.

Figure 45. Comparison of shear stresses, static shear test 3, SFB-3.

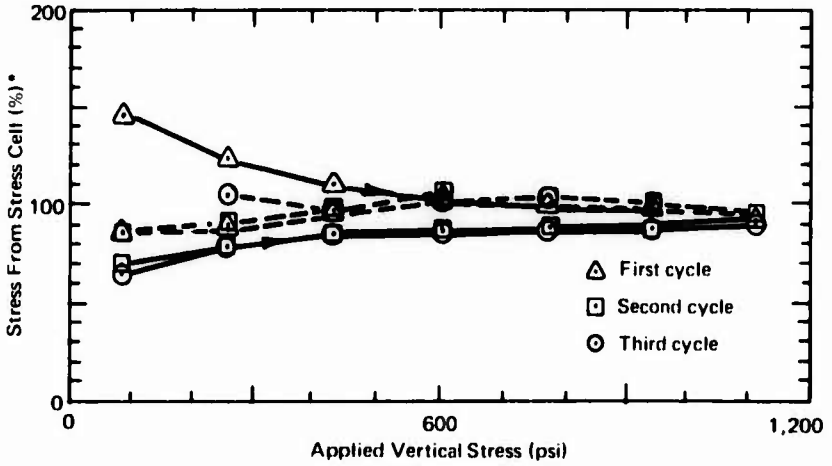

*Percent of applied vertical stress.

Figure 46. Comparison of vertical stresses, static shear test 1, SFB-4.

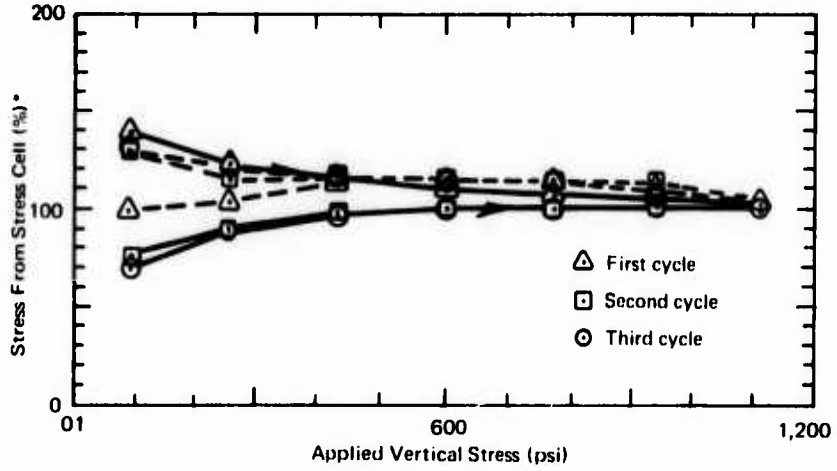

*Percent of applied vertical stress.

Figure 47. Comparison of vertical stresses, static shear test 2, SFB-5.

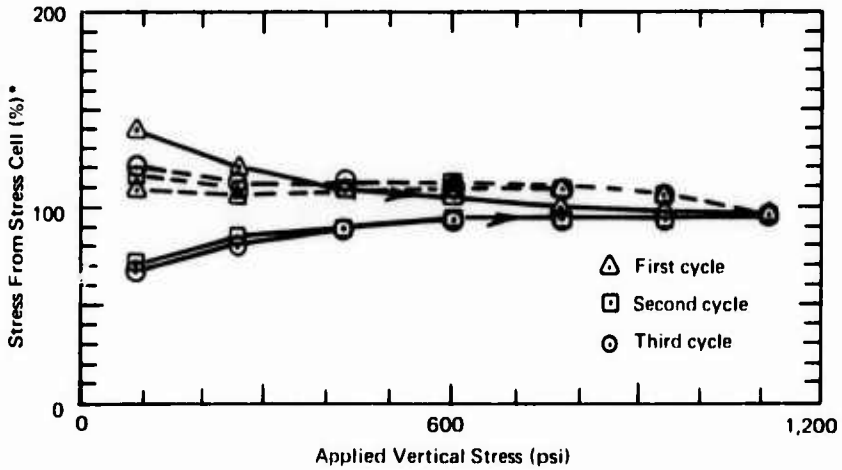

*Percent of applied vertical stress.

Figure 48. Comparison of vertical stresses, static shear test 3, SFB-3.

Dynamic Tests

General. The objective of the dynamic tests was to evaluate the dynamic response of the stress cell in sand under a blast environment. Only the response of the stress cell to normal stress was evaluated in these tests. The stress influence coefficients and equations used in the computation of soil stresses from the stress cell data were the same as those used in the static normal tests because the dry sand used in the tests is essentially insensitive to strain rate.

Tests in Blast Simulator. Data from a given strain gage in the stress cell for different tests have the same wave shape; however, their magnitudes varied somewhat from test to test. Typical data from the stress cell and the pressure transducer are presented in Figure 49. From Figure 49, it is apparent that, except for the first 10 msec, the wave forms of the data from the stress cell and those from the pressure transducer are similar. The pronounced oscillations in the stress cell data during the first 10 msec were caused by the response of the blast simulator and the pipe containing the sand (Figure 13). Vertical and horizontal stresses were computed from the stress cell data at various selected times. Precise determination of stresses from the stress cell data immediately after the arrival of the stress wave, however, was not possible because the strain data from the stress cell were masked by the reflections from the blast simulator and the pipe. All initial data peaks, consequently, were obtained by backward extrapolation (dotted lines in Figure 49). Vertical stresses from the stress cell at the three selected times (5, 30, and 60 msec) were compared with the corresponding dynamic pressures from the pressure transducer located 5-1/2 inches above the level of the stress cell (Figure 50). It can be seen from Figure 50 that the three data points for each test, except for test 8, are closely grouped; this demonstrates that the response of the stress cell follows the decay of the overpressure pulse. A more detailed comparison of the vertical stress from the stress cell with the applied dynamic pressure for all tests is presented in Figure 51. The vertical stresses from the stress cell are generally within 15% absolute of the applied dynamic pressures. The average earth pressure coefficient at rest computed from the stress cell data is 0.37.

Tests at Point Mugu. After each test at Point Mugu, the cavity inside the steel cylinder (Figure 14) was filled with damp sand from the surcharge above. The plywood box lid, initially placed on the top of the cylinder, was adjacent to the cylinder with its bottom side up. A hole about 14 inches in diameter was cut in the bottom side of the plywood box lid. After removing the damp sand in the cylinder with a plastic scoop, it was found that the

original dry sand surface had moved upward about 6 inches with respect to the top of the tank. The sand surface had a rather fluffy appearance. Moreover, the stress cells moved upward along with the surrounding sand, with their **Z**-strain gages tilted slightly toward the wall of the tank. These observed upward displacements, apparently, were caused by the reflected wave from the water table below (Figure 14). After test 3, stress cell SFB-4 had a small, superficial crack at the base of the handle; however, all its strain gages were still functioning satisfactorily. This cracking, caused by a high bending moment at that location, may be avoided in future experiments by providing the stress cell with a 1-inch handle instead of the 2-1/2-inch handle used. Stress cell SFB-3 was not damaged.

No useful data were obtained from the first test because the instrumentation was not grounded properly. Data were obtained for all other tests.

The data from corresponding pressure gages used in tests 2 and 3 were similar. The data from corresponding gages within the stress cells for each test were also similar. Strain data from the **Z**-strain gage in SFB-3, for example, were similar to the corresponding data from SFB-4. Typical data from these two tests are presented in Figure 52. The wave shapes of the overpressure data and the stress cell data are somewhat similar.

Vertical stresses computed from the stress cell data were compared with the applied dynamic pressure (Figure 53). From Figure 53, it is apparent that the stresses from the stress cell are only about one-fourth those from the pressure transducer. This large difference in magnitudes may have been caused by spatial attenuation. To explore this possibility, consider the contour plot of the vertical stresses below a circular footing subjected to a unit pressure (Figure 54). The diameter of the circular footing is 14 inches, the same dimension as the hole cut in the bottom of the plywood box lid of the test chamber. Locations of the stress cells are plotted to scale, corresponding to their actual locations below the sand surface (Figure 14) inside the tank. Clearly, the vertical stress at the location of the stress cells is only about 24% of the applied stress on top. The diameter of the pressure front, because the 8-inch-diameter explosive charge was placed at only 1 foot above the sand surface, was probably only slightly more than 14 inches when it hit the surface of the sand. The vertical stresses from the stress cell, as a consequence, are only about one-quarter of the applied dynamic pressures. The vertical stress from the stress cell (Figure 53) became zero at 3.5 msec, when the reflected stress wave arrived from the water table below.

The validity of dynamic field measurements from the stress cell is still open to question. Further dynamic testing of the stress cell should be accomplished to resolve the remaining uncertainties.

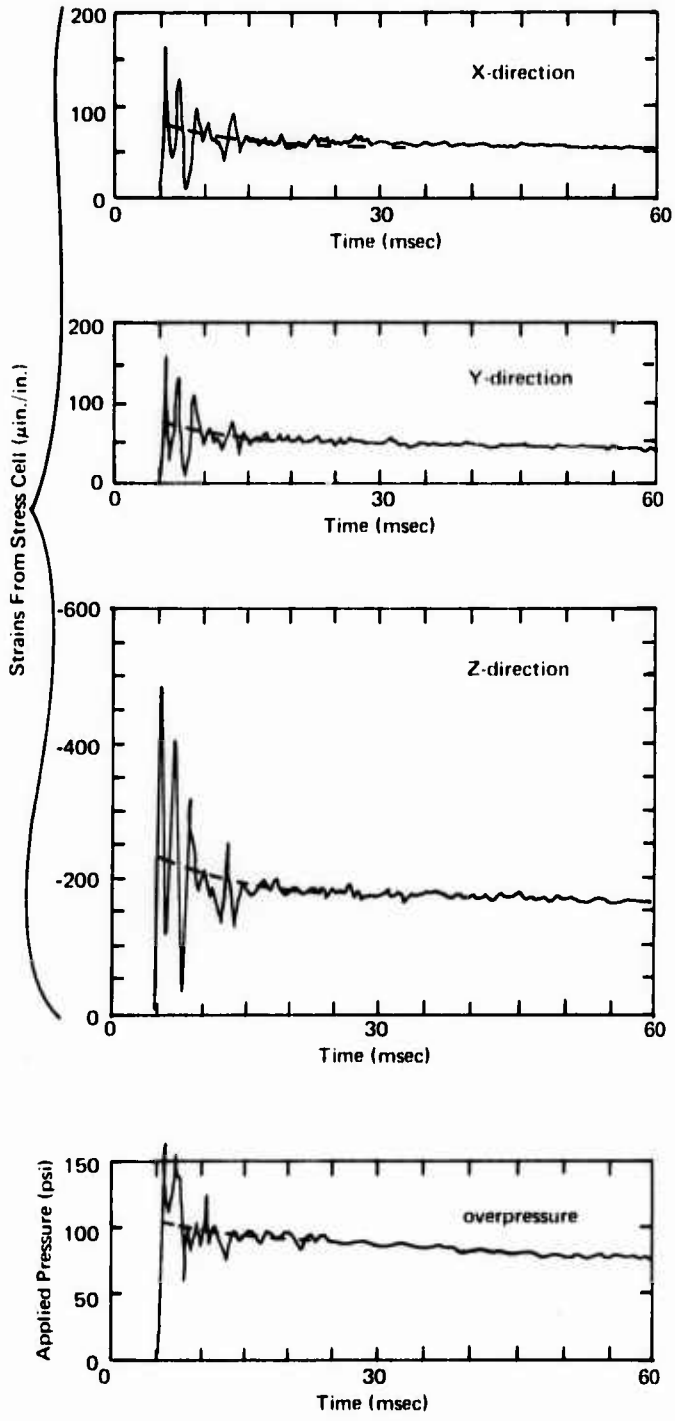

Figure 49. Typical stress cell data and overpressure data from dynamic tests in NCEL blast simulator, SFB-1.

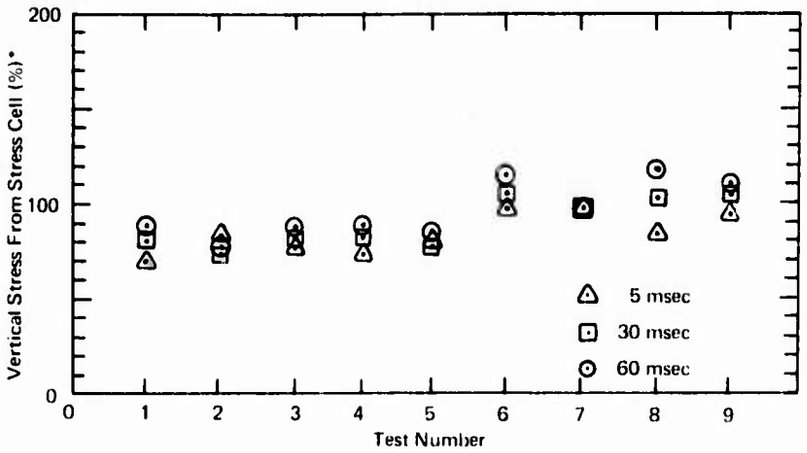

*Percent of applied dynamic pressure

Figure 50. Comparison of vertical stresses, dynamic tests in NCEL blast simulator, SFB-1.

FINDINGS AND CONCLUSIONS

The purpose of the experiments reported was to evaluate the adequacy of cue-ball stress cells for measuring the complete state of stress at a point in a soil field under static or dynamic loading. Their operation is based on the deductions from elastic theory that: (1) the response of a stiff spherical inclusion is insensitive to changes in the stiffness of the encompassing solid provided that the modulus of elasticity of the inclusion is about 10 or more times the maximum corresponding value for the solid, and (2) the stresses along a given direction in the inclusion are essentially constant.

The test results and analysis indicate that:

1. The stress cell requires no calibration.
2. The stress cell behaves linearly under hydrostatic pressures to 3,000 psi in water.
3. Embedded foil strain gages in the stress cell have negligible influence on the strain field within the stress cell.
4. The stress cell response is insensitive to changes in soil moduli for static stresses up to 1,110 psi.

5. Static normal stress and shear stress measurements are generally within ±10% of the actual stresses.

6. Law of stress transformation can be applied to stress measurements from the stress cell.

7. The dynamic response of the stress cell follows the rise and decay of the applied dynamic pressure pulse.

8. Dynamic stress measurements from the stress cell are generally with ±15% of the corresponding pressure in the blast simulator.

9. Accuracy of dynamic measurements from the stress cell in field experiments is still uncertain.

In brief, the cue-ball stress cells are excellent gages for making static measurements in sand, but their adequacy for dynamic measurements requires further evaluation.

RECOMMENDATIONS

1. Shorten the handle of the stress cell from 2-1/2 inches to 1 inch.

2. Test the dynamic response of the stress cell more rigorously in the laboratory and in the field.

3. Test a FM unit that puts six channels of dynamic data into one channel made specially for the stress cell.

ACKNOWLEDGMENT

Mr. O. J. Olsen fabricated and tested the first cue-ball stress cell, SFB-1. Mr. D. T. Corrente assisted in the fabrication and testing of the stress cells (SFB-2, SFB-3, SFB-4, and SFB-5). Mr. J. R. Allgood gave numerous valuable suggestions.

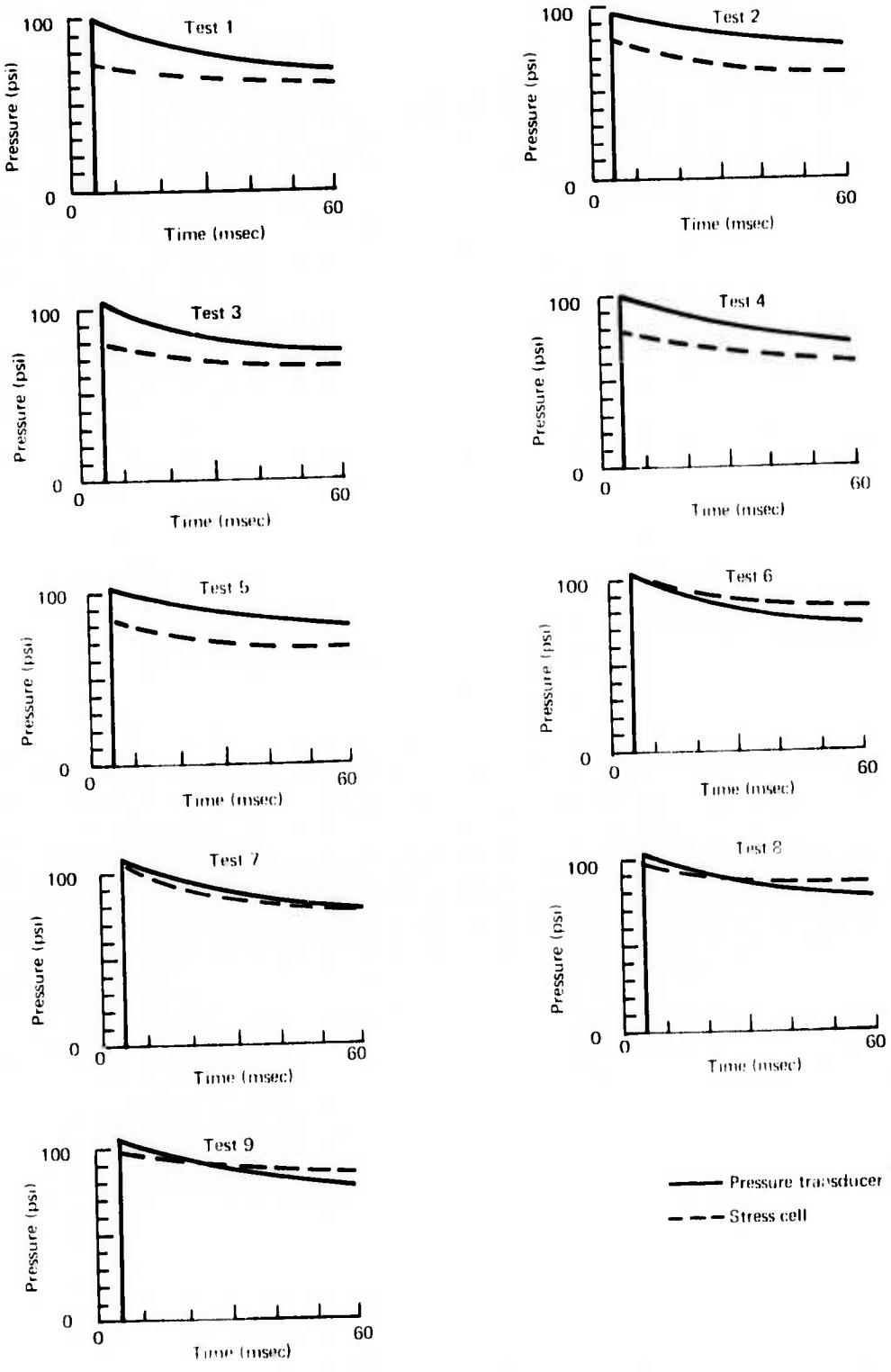

Figure 51. Detailed comparison of vertical stresses, dynamic tests in NCEL blast simulator, SFB-1.

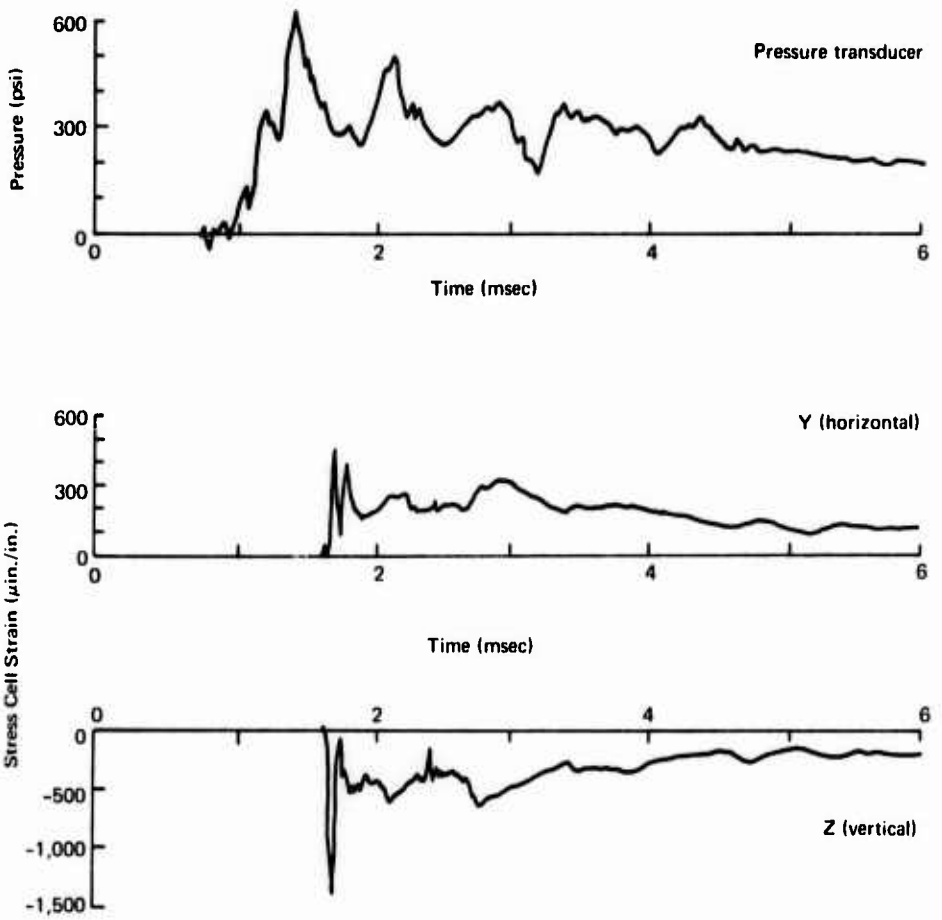

Figure 52. Typical dynamic data from tests at Point Mugu.

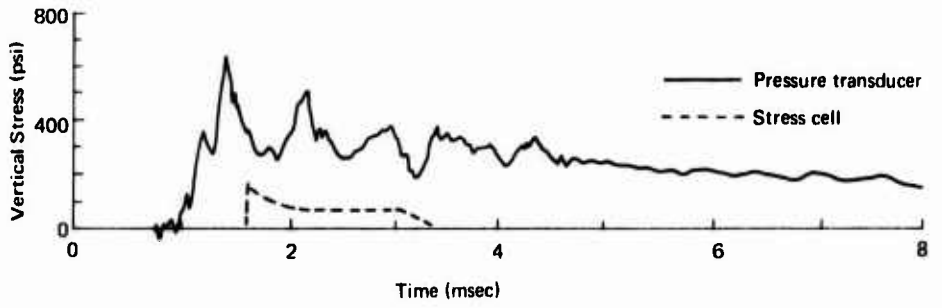

Figure 53. Comparison of vertical stresses, dynamic tests at Point Mugu.

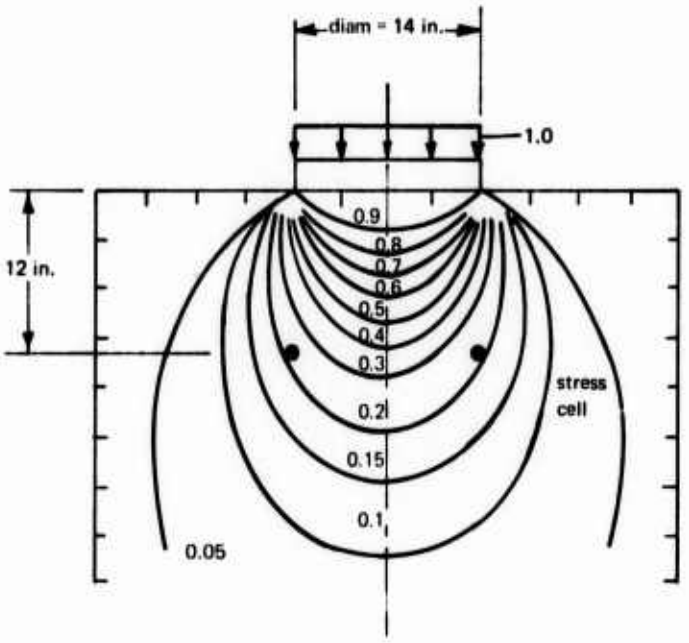

Figure 54. Distribution of vertical stresses under a circular footing.

Appendix

CONFIGURATION OF STRAIN GAGES IN STRESS CELLS

Nine strain gages are embedded in each stress cell as shown in Figure 8. Under normal operating conditions (that is, when the complete state of stress at a point in soil is required), only the **X**, **Y**, **Z**, **XY45**, **YZ45**, and **ZX45** are monitored. Furthermore, only **X**, **Y**, and **Z** gages are monitored in special situations where only normal stresses are required. The 135 gages (**XY135**, **YZ135**, and **ZX135**) are redundant and not used unless one or more of the other gages do not function. These 135 gages, however, may be used if the user desires to obtain extra data for checking purposes. An additional orthogonality check (the sum of three mutually orthogonal strains at a point in an elastic, isotropic, and homogeneous solid is a constant) can be obtained if one of the 135 gages is monitored in normal operating conditions. Otherwise, only one orthogonal check can be obtained under normal operating conditions when the 135 gages are not monitored.

Moreover, one or more of the strain gages (**X**, **Y**, **Z**, **XY45**, **YZ45**, and **ZX45**) may be damaged accidentally. If this occurs, one or a combination of alternative setups can be used to obtain the required strains as follows:

1. One or more of the 45 gages not working, and the **X**, **Y**, and **Z** gages working—use the **X**, **Y**, and **Z** gages, and substitute the appropriate 135 gage for the corresponding 45 gage that is not working. For example, the **XY135** gage is used when the **XY45** gage does not work. Compute the required shearing strain from one of the following equations:

$$\gamma_{XY} = \epsilon_X + \epsilon_Y - 2\epsilon_{XY135} \tag{24}$$

$$\gamma_{YZ} = \epsilon_Y + \epsilon_Z - 2\epsilon_{YZ135} \tag{25}$$

$$\gamma_{ZX} = \epsilon_Z + \epsilon_X - 2\epsilon_{ZX135} \tag{26}$$

2. **X** gage not working—use the **Y**, **Z**, **XY45**, **YZ45**, and **XZ45** gages. Use the **YZ135** or **XZ135** gage, whichever is appropriate. Compute the normal strain in the **X**-direction with one of the equations below:

$$\epsilon_X = \epsilon_{XY45} + \epsilon_{XY135} - \epsilon_Y \tag{27}$$

$$\epsilon_X = \epsilon_{ZX45} + \epsilon_{ZX135} - \epsilon_Z \tag{28}$$

Compute the required shearing strains as indicated in the text.

3. **Y** gage not working—use the **X**, **Z**, **XY45**, and **YZ45** and **ZX45** gages. In addition, use the **YZ135**, or the **XY135** gage. Compute the normal strain in the **Y**-direction with one of the following equations:

$$\epsilon_Y = \epsilon_{YZ45} + \epsilon_{YZ135} - \epsilon_Z \quad (29)$$

$$\epsilon_Y = \epsilon_{XY45} + \epsilon_{XY135} - \epsilon_X \quad . (30)$$

Compute the required shearing strain as indicated in the text.

4. **Z** gage not working—use the **X**, **Y**, **XY45**, **YZ45**, and **ZX45** gages. Also, use the **YZ135** gage or the **ZX135** gage. Use one of the following equations to compute the normal strain in the **Z**-direction.

$$\epsilon_Z = \epsilon_{YZ45} + \epsilon_{YZ135} - \epsilon_Y \quad (31)$$

$$\epsilon_Z = \epsilon_{ZX45} + \epsilon_{ZX135} - \epsilon_X \quad (32)$$

Again, compute the required shearing strains as indicated in text.

REFERENCES

1. Naval Civil Engineering Laboratory. Technical Note N-1131: The development of a three-dimensional stress cell for granular soils: Preliminary evaluation, by T. K. Lew. Port Hueneme, Calif., Oct. 1970. (AD 714837)

2. A. Coutinho. "Theory of an experimental method for determining stresses, not requiring an accurate knowledge of the modulus of elasticity," in International Association for Bridge and Structural Engineering, Publications, vol. 9, Zurich, Switzerland, 1949, pp. 83-93.

3. J. N. Goodier. "Concentration of stress around spherical and cylindrical inclusions and flaws," Journal of Applied Mechanics, vol. 1, no. 2, June 1933, pp. 39-44.

4. E. L. Wilson. "Structural analysis of axisymmetric solids," AIAA Journal, vol. 3, no. 12, Dec. 1965, pp. 2269-2274.

5. R. C. Dove, R. I. Brasier, and W. E. Baker. "Selection of gages for strain measurement at interior points," Experimental Mechanics, vol. 2, no. 6, June 1962, pp. 189-190.

6. W. E. Baker and R. C. Dove. "Construction and evaluation of a three-dimensional strain rosette," Experimental Mechanics, vol. 3, no. 9, Sept. 1963, pp. 201-206.

7. W. A. Shaw and J. R. Allgood. "An atomic blast simulator," Society for Experimental Stress Analysis, Proceedings, vol. 17, no. 1, 1959, pp. 127-134.

8. A. J. Hendron. The behavior of sand in one-dimensional compression, Ph.D. thesis, University of Illinois. Urbana, Ill., 1963.

9. Naval Civil Engineering Laboratory. Technical Report R-582: Influence of soil modulus on the behavior of cylinders buried in sand, by J. R. Allgood, J. B. Ciani, and T. K. Lew. Port Hueneme, Calif., June 1968. (AD 670477)

10. A. J. Durelli, E. A. Phillips, and C. H. Tsao. Introduction to the theoretical and experimental analysis of stress and strain. New York, McGraw-Hill, 1958, chaps. 2 and 3, pp. 36-80.

LIST OF SYMBOLS

C_c	Lateral stress concentration factor
C_s	Direct stress concentration factor
e	Volumetric strain
E_c	Young's modulus for inclusion
E_h	Young's modulus for host material
G	Shear modulus for inclusion
k	Lateral–normal stress influence coefficient
K	Direct–normal stress influence coefficient
K_o	Ratio between horizontal and vertical stress
K_s	Shear stress influence coefficient
X	Strain gage along X-axis of stress cell
XY45, XY135	Strain gages in XY-plane of stress cell
Y	Strain gage along Y-axis of stress cell
YZ45, YZ135	Strain gages in YZ-plane of stress cell
Z	Strain gage along Z-axis of stress cell
ZX45, ZX135	Strain gages in ZX-plane of stress cell
$\epsilon_X, \epsilon_Y, \epsilon_Z$	Normal strain components in inclusion
$\epsilon_{XY45}, \epsilon_{YZ45}, \epsilon_{ZX45}$	Strain components from 45-degree gage in each reference plane of stress cell
$\gamma_{XY}, \gamma_{YZ}, \gamma_{ZX}$	Shearing strain components in reference planes of inclusion
λ	Lamé's constant
$\sigma_{Xc}, \sigma_{Yc}, \sigma_{Zc}$	Normal stress components in inclusion
$\sigma_{Xh}, \sigma_{Yh}, \sigma_{Zh}$	Normal stress components in host material
$\tau_{XYc}, \tau_{YZc}, \tau_{ZXc}$	Shear stress components in inclusion
$\tau_{XYh}, \tau_{YZh}, \tau_{ZXh}$	Shear stress components in host material
ν_c	Poisson's ratio of inclusion
ν_h	Poisson's ratio of host material